

Producing slow light in warm alkali vapor using electromagnetically induced transparency

Kenneth DeRose, Kefeng Jiang, Jianqiao Li, et al.

Citation: *American Journal of Physics* **91**, 193 (2023); doi: 10.1119/5.0128967

View online: <https://doi.org/10.1119/5.0128967>

View Table of Contents: <https://aapt.scitation.org/toc/ajp/91/3>

Published by the [American Association of Physics Teachers](#)

ARTICLES YOU MAY BE INTERESTED IN

[A shorter path to some action variables](#)

American Journal of Physics **91**, 177 (2023); <https://doi.org/10.1119/5.0118683>

[An exploration of circumbinary systems using gravitational microlensing](#)

American Journal of Physics **91**, 182 (2023); <https://doi.org/10.1119/5.0088604>

[Is contour integration essential? Alternatives for beginning physics students](#)

American Journal of Physics **91**, 170 (2023); <https://doi.org/10.1119/5.0084475>

[From Sackur–Tetrode entropy to the ideal gas adiabatic equation in one step](#)

American Journal of Physics **91**, 247 (2023); <https://doi.org/10.1119/5.0139175>

[A tabletop experiment for speed of light measurement using a Red Pitaya STEMLab board](#)

American Journal of Physics **91**, 206 (2023); <https://doi.org/10.1119/5.0099720>

[Thermal infrared astronomy for the introductory laboratory](#)

American Journal of Physics **91**, 122 (2023); <https://doi.org/10.1119/5.0081072>



Advance your teaching and career
as a member of **AAPT**

LEARN MORE





Producing slow light in warm alkali vapor using electromagnetically induced transparency

Kenneth DeRose, Kefeng Jiang, Jianqiao Li, Macbeth Julius, Linzhao Zhuo, Scott Wenner,^{a)} and Samir Bali^{b)}

Department of Physics, Miami University, Oxford, Ohio 45056-1866

(Received 2 October 2022; accepted 27 November 2022)

We present undergraduate-friendly instructions on how to produce light pulses propagating through warm Rubidium vapor with speeds less than 400 m/s, i.e., nearly a million times slower than c . We elucidate the role played by electromagnetically induced transparency (EIT) in producing slow light pulses and discuss how to achieve the required experimental conditions. The optical setup is presented, and details provided for preparation of pump, probe, and reference pulses of the required size, frequency, intensity, temporal width, and polarization purity. EIT-based slow light pulses provide the most widely studied architecture for creating quantum memories. Therefore, the basic concepts presented here are useful for physics and engineering majors who wish to get involved in the development of cutting-edge quantum technologies. © 2023 Published under an exclusive license by American Association of Physics Teachers.

<https://doi.org/10.1119/5.0128967>

I. INTRODUCTION

It has been two decades since the first demonstration of slow optical pulses propagating through atomic media.^{1,2} Slow light was revealed as the striking consequence of a quantum mechanical phenomenon in light–matter interaction known as EIT, i.e., electromagnetically induced transparency. EIT arises from the interference between probability amplitudes for absorption pathways that are simultaneously excited by two resonant light fields—one strong, referred to as the pump (or coupling) field, and the other weak, referred to as the probe.^{3,4} EIT and slow light in warm alkali vapor continue to be central topics of research in quantum information and quantum technology, particularly for building robust quantum memories,^{5–7} and stable photon-shot-noise-limited electromagnetic field sensors using Rydberg atoms.⁸ In Ref. 6, for instance, the authors provide an overview of current approaches to quantum memory and state that “although all of these approaches have been studied and demonstrated, EIT remains the most popular scheme for quantum memory,” because, “in comparison to the other approaches, the EIT approach has a long storage time and is a relatively easy-to-implement and inexpensive solution.”

An excellent article on EIT-based experiments for undergraduate laboratories was published just over a decade ago.⁹ Elegant EIT-based experiments carried out at undergraduate institutions have also been reported.¹⁰ However, an undergraduate-friendly experimental description of slow light in atomic vapor does not exist. In this paper, we endeavor to fill this gap. This is important because an increasing number of physics and engineering majors wish to get involved in the development of cutting-edge quantum technologies.

There are several pedagogical advantages to introducing the concepts of EIT and slow light in an optics class for undergraduate seniors and first/second-year graduate students. For instance, in the advanced lecture/lab course “Optics and Laser Physics” that we teach at Miami University, students often ask, “We’ve read about laser applications in imaging, communications and medicine... can you tell us about quantum applications we haven’t heard

of?” EIT and slow light can provide a satisfying answer to this question. EIT physics is a natural extension to what these students have already learned about light–matter interaction. Early in the semester, they are introduced to population-rate equations for a laser system, which sets the stage for an EIT-based slow light system, since the simplest model for either system is provided by a three-level atom. Furthermore, students know about group versus phase velocity, and therefore have all the necessary background to learn about how a steep positive gradient of the refractive index within a narrow EIT spectral window can lead to a dramatically slow group velocity.

In this article, we state the relevant theoretical results for EIT and slow light, and describe our experimental setup for producing slow light pulses with group velocities less than 400 m/s. A price list for parts is included in the online supplementary material.¹¹

II. THEORETICAL DESCRIPTION

The theory behind EIT and slow light has been explained in several high-quality undergraduate-friendly articles (see, for example, Refs. 9 and 12–15) including a textbook-treatment in Ref. 16, which is amenable to seniors. Here, we summarize the relevant results. A more complete derivation can be found in the online supplementary material.¹¹

A. Three-level atom model

Following the treatment in Ref. 16, we depict a fictitious three-level atom in Fig. 1, in which transitions are allowed between states 1 and 3 and between states 2 and 3, but not between states 1 and 2. This is the so-called lambda-system because the lower levels 1 and 2 have close-lying energies, resulting in a Λ -shaped configuration. The energy differences between levels 3 and 1, 3 and 2, and 2 and 1 are $\hbar\omega_{31}$, $\hbar\omega_{32}$, and $\hbar\omega_{21}$, respectively. The standard EIT experiment consists of a sample of such atoms illuminated by a strong coupling (or pump) laser of frequency ω_c and a weak probe laser of frequency ω_p , both tuned to near-resonance with $|3\rangle$ from levels $|2\rangle$ and $|1\rangle$ respectively. The laser detunings are $\Delta_c \equiv \omega_c - \omega_{32}$ and $\Delta_p \equiv \omega_p - \omega_{31}$. We assume that

the pump beam only addresses the coupling transition $|2\rangle \rightarrow |3\rangle$ and the probe beam only addresses the $|1\rangle \rightarrow |3\rangle$ transition. This may be satisfied by ensuring that the interaction between the pump beam and the probe transition, and vice versa, is forbidden by quantum mechanical selection rules (as in Zeeman EIT, discussed in detail in Sec. III A below). Alternatively, this interaction may be negligible because the two transitions ω_{31} and ω_{32} are significantly different (as in hyperfine EIT, see Sec. III A). In either situation, the pump frequency is fixed, while the probe frequency is scanned so that the two-photon detuning Δ' , defined as $\Delta' \equiv \Delta_p - \Delta_c = \omega_p - \omega_c - \omega_{21}$, passes through zero (two-photon resonance). The probe absorption is measured as a function of this scanning probe frequency.

In the supplementary material, Secs. S1A and S1B,¹¹ we write the Hamiltonian for an illuminated three-level atom, assuming that the incident field-induced electric dipole is the predominant light-atom interaction. We calculate the eigenenergies and eigenstates in Eqs. (S9)–(S11), taking the pump and probe beams to be on-resonance for simplicity (i.e., the two-photon detuning Δ' is zero). One of the eigenstates is a “dark” state, which is a coherent superposition of the two ground states $|1\rangle$ and $|2\rangle$. This dark state has no quantum overlap with the excited state $|3\rangle$. Thus, an atom, once it is transferred to the dark state upon interaction with the light fields, stays there, no longer able to absorb a probe photon. In general, for non-zero detunings Δ_p and Δ_c , the steady-state dark state is formed at two-photon resonance $\Delta' = 0$. Note that in the absence of the pump, the weak resonant probe would be completely absorbed. Thus, the pump laser “coherently prepares” the atoms to be transparent to the probe—this is EIT.

In order to calculate the spectral width of the transparency window, we must take into account the decay of the light-induced dipole moment due to various decohering processes (also called damping, or relaxation, processes). Such processes may arise from atomic motion which may, for example, cause the atom to leave the illuminated region, and the light-atom interaction to cease altogether. Similarly, elastic and inelastic collisions with other atoms and with the container walls, and other processes such as spontaneous emission, affect the phase and amplitude of the light-induced dipole moment. These mechanisms are discussed in more detail in Secs. III B and III C below. We denote all decay processes from $3 \rightarrow 1$ and from $3 \rightarrow 2$ by the optical decoherence rates γ_{13} and γ_{23} , respectively. The two ground states are close-lying, so that non-optical processes, such as collisions, may suffice to cause interchange between the two states—we denote this two-way $1 \leftrightarrow 2$ decay by the ground state decoherence rate γ_{12} . In dilute samples where the densities are not so high, non-optical damping processes (e.g., collisions between ground state atoms) begin to dominate over

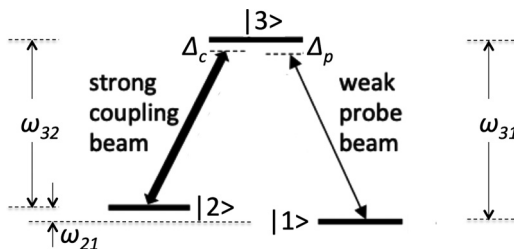


Fig. 1. Three-level atom in the Λ -shaped configuration.

optical damping processes e.g., spontaneous emission or Doppler broadening, γ_{12} is much smaller than γ_{13} and γ_{23} . This is an important requirement for EIT which is satisfied in our experiments, see Sec. III C below.

We show in Secs. S1C–S1D of the supplementary material¹¹ that the density matrix formalism allows for simple phenomenological inclusion of decay processes into the calculation of the probe-induced atomic dipole moment and polarizability. This allows us to deduce the complex refractive index $n(\omega_p) = n_r(\omega_p) + in_i(\omega_p)$. The imaginary part n_i yields the absorption spectrum $\alpha(\omega_p)$. The complex refractive index is a convenient way to express something well known: Where there is dispersion $n_r(\omega)$, there must be absorption α . This is owing to causality-based Kramers–Kronig relations between the real and imaginary parts of the refractive index.¹⁷ We calculate the absorption $\alpha(\omega_p)$ and real refractive index $n_r(\omega_p)$ seen by the weak probe (see Eqs. (S22) and (S23)) propagating through a sample of Λ -atoms, which is coherently prepared by a strong pump beam in a dark state, as mentioned above. In Secs. II B and II C below, we discuss some important limiting situations which will be probed by experiments.

B. Absorption and refractive index with pump field off

When the coupling field (or pump) is off, no EIT occurs. We obtain the usual results for probe absorption and real refractive index, which are plotted in Figs. 2(a) and 2(b),

$$\alpha \xrightarrow{\Omega_c=0} \frac{N\omega_p}{\epsilon_0 c} \frac{|\mu_{13}|^2}{\hbar} \frac{\gamma_{13}}{\Delta_p^2 + \gamma_{13}^2}, \quad (1)$$

$$n_r \xrightarrow{\Omega_c=0} 1 - \frac{N}{2\epsilon_0} \frac{|\mu_{13}|^2}{\hbar} \frac{\Delta_p}{\Delta_p^2 + \gamma_{13}^2}. \quad (2)$$

Here, Ω_c is the coupling beam Rabi frequency defined as $\Omega_c \equiv \vec{d}_{32} \cdot \vec{\epsilon}_c E_c / 2\hbar$, where \vec{d}_{32} is the transition dipole moment between levels $|2\rangle$ and $|3\rangle$, $\vec{\epsilon}_c$ is the unit polarization vector in the direction of the coupling electric field, and \hbar is

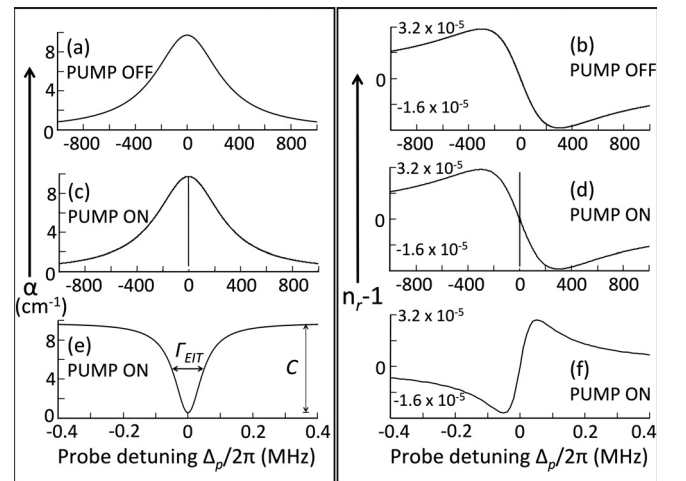


Fig. 2. The probe absorption coefficient α (left panel) in cm^{-1} and real refractive index n_r (right panel), versus probe detuning $\Delta_p = \omega_p - \omega_{31}$ as predicted by Eqs. (1)–(4). (a) and (b) The case of “no pump” from Eqs. (1) and (2). (c) and (d) The “EIT case” from Eqs. (3) and (4) with parameter values from our experiments: $\Delta_c = 0$, $|\Omega_c|/2\pi = 4$ MHz, $\omega_p/2\pi = 3.77 \times 10^{14}$ Hz, $N = 3.36 \times 10^{11}/\text{cm}^3$, $\gamma_{13}/2\pi = 300$ MHz, $\gamma_{12}/2\pi = 3$ kHz, $|\mu_{13}| = 2.54 \times 10^{-29}$ C.m. (e) and (f) Magnified view of sharp EIT features in (c) and (d).

Planck's constant divided by 2π .¹⁸ N is the number of atomic dipoles per unit volume, c is the speed of light in vacuum, ϵ_0 is the electric permittivity of vacuum, and μ_{13} is defined as the projection of the induced probe dipole moment on the direction of the probe field polarization.

Equation (1), plotted in Fig. 2(a), depicts the expected Lorentzian absorptive line shape, with a half width at half maximum (HWHM) γ_{13} and a maximum at $\Delta_p = 0$. Equation (2), plotted in Fig. 2(b), depicts the expected dispersive line shape around probe-resonance, again with a HWHM of γ_{13} . In the immediate vicinity of resonance $\Delta_p \approx 0$, we see that $n_r \rightarrow 1 - N|\mu_{13}|^2\Delta_p/(2\epsilon_0\hbar\gamma_{13}^2)$, i.e., $n_r(\omega_p)$ has a negative slope. This is the well-known ‘‘anomalous dispersion’’ effect that occurs close to an atomic resonance and in which n_r decreases with increasing optical frequency. By contrast, as we move further away from resonance we see that n_r increases with frequency on either side. This is the normal dispersion, consistent with the classic experiment of propagating white light through a glass prism and observing that red light deviates the least and blue the most.

C. Absorption and refractive index with pump field on

When the strong coupling field is on, and assumed to be on-resonance for simplicity ($\Delta_c = 0$), we obtain for the probe absorption $\alpha(\omega_p)$ and real refractive index $n_r(\omega_p)$ in the ‘‘weak-probe approximation’’ ($\Omega_p \ll \Omega_c$; here, Ω_p is the probe Rabi frequency and is defined as $\Omega_p \equiv \vec{d}_{31} \cdot \vec{\epsilon}_p E_p / 2\hbar$, where \vec{d}_{31} is the transition dipole moment between levels $|1\rangle$ and $|3\rangle$, and $\vec{\epsilon}_p$ is the unit polarization vector in the direction of the probe electric field¹⁸),

$$\alpha(\omega_p) = \frac{N\omega_p |\mu_{13}|^2}{\epsilon_0 c \hbar} \times \frac{\gamma_{13}\Delta_p^2 + \gamma_{12}(\gamma_{12}\gamma_{13} + |\Omega_c|^2)}{\left[\Delta_p^2 - \gamma_{12}\gamma_{13} - |\Omega_c|^2\right]^2 + \Delta_p^2[\gamma_{12} + \gamma_{13}]^2}, \quad (3)$$

$$n_r(\omega_p) = 1 - \frac{N |\mu_{13}|^2}{2\epsilon_0 \hbar} \times \frac{\Delta_p(\Delta_p^2 - |\Omega_c|^2 + \gamma_{12}^2)}{\left[\Delta_p^2 - \gamma_{12}\gamma_{13} - |\Omega_c|^2\right]^2 + \Delta_p^2[\gamma_{12} + \gamma_{13}]^2}. \quad (4)$$

Equations (3) and (4) are plotted in Figs. 2(c)–2(f). Equations (S22) and (S23) are generalized forms of Eqs. (3) and (4) for $\Delta_c \neq 0$.

The absorption α and refractive index n_r in the lower panels of Fig. 2 are strikingly different from the top panel where the coupling field is off. It is instructive to verify that Eqs. (1)–(4) satisfy the Kramers–Kronig relations.¹⁷

D. The EIT ‘‘window’’

EIT manifests itself as a dramatic drop in the absorption $\alpha(\omega_p)$ in Figs. 2(c) and 2(e) when the coupling and probe beams are on-resonance. In our experiments, $\gamma_{12}/2\pi \sim$ few kHz, $|\Omega_c|/2\pi \sim$ few MHz, $\gamma_{13}/2\pi \sim$ few hundred MHz, and $|\Delta_p|/2\pi \leq 100$ kHz, so that we verify the ‘‘strong coupling field approximation,’’

$$|\Omega_c| \gg |\Delta_p|, \gamma_{12}, \quad (5)$$

which is one of two conditions (see Eq. (11) below) that Ω_c must satisfy in order to produce slow light. Using $\gamma_{12} \ll \gamma_{13}$, we find from Eq. (3), in the $\Delta_p \rightarrow 0$ limit,

$$\alpha \rightarrow \frac{N\omega_p |\mu_{13}|^2}{\epsilon_0 c \hbar} \frac{\gamma_{12}}{|\Omega_c|^2} \approx 0, \quad (6)$$

which yields transparency in a narrow ‘‘EIT window.’’

A simple approximate expression for the EIT linewidth Γ_{EIT} (see Fig. 2(e)) may be obtained by setting $\Delta_p = 0$ in Eq. (S22) while allowing Δ_c to vary around the two-photon resonance condition $\Delta_p - \Delta_c = 0$,

$$\alpha \xrightarrow{\Delta_p=0} \alpha_{\Omega_c=0} \left[1 - \frac{|\Omega_c|^2}{\gamma_{13}} \frac{\gamma_{12} + \frac{|\Omega_c|^2}{\gamma_{13}}}{\Delta_c^2 + \left(\gamma_{12} + \frac{|\Omega_c|^2}{\gamma_{13}}\right)^2} \right], \quad (7)$$

where $\alpha_{\Omega_c=0} = N\omega_p|\mu_{13}|^2/(\epsilon_0 c \hbar \gamma_{13})$ is obtained by setting $\Delta_p = 0$ in Eq. (1). The first term inside the parentheses in Eq. (7) represents the baseline absorption without EIT. The second term is the EIT window depicted in Fig. 2(e), which is a Lorentzian with full-width-half-maximum Γ_{EIT} given by

$$\Gamma_{\text{EIT}} = 2 \left(\gamma_{12} + \frac{|\Omega_c|^2}{\gamma_{13}} \right). \quad (8)$$

In Eq. (8), Ω_c depends on the pump intensity I (see Eq. (16) below), so that the EIT window broadens when the intensity of the pump beam increases. Upon substituting typical experimental parameter values (see caption under Fig. 2) into the approximate expression in Eq. (8), we predict $\Gamma_{\text{EIT}} \approx 100$ kHz for the EIT window. This is in close agreement with Eq. (3), which is plotted in Fig. 2(e). The probe absorption α is minimum when Δ_c is minimum, so that an expression for the EIT contrast, or amplitude of the transparency window, denoted by C (see Fig. 2(e)) may be simply obtained by setting $\Delta_c = 0$ in the second term of Eq. (7): $C = |\Omega_c|^2 / (\gamma_{13}\gamma_{12} + |\Omega_c|^2)$ which, for the typical experimental-parameter values in the Fig. 2 caption, predicts $\approx 100\%$ transparency.

In practice, the observed contrast and linewidth are much lower (see Sec. VI). This is because, in steady-state, the fraction of atoms settling in the dark state is significantly reduced for reasons discussed in Sec. III B. In short, our theory is based on a closed three-level model, whereas, in real atoms, many energy levels are addressed by the laser fields. This provides extraneous energy-levels to which the population can leak, severely reducing contrast (in our experiments the maximum contrast is about 25%). The lowered contrast, in turn, leads to a significant reduction in the observed EIT linewidth: Only the probe spectral components that lie at the center of the EIT window can propagate through and are detectable in transmission (though considerably reduced in intensity), while frequency components near the edge of the window are too heavily attenuated to be detected.^{19,20} Moreover, in Ref. 19 it is shown that the power-broadened component of the linewidth in Eq. (8) is estimated to reduce by a factor \sqrt{OD} , where OD is the on-resonance optical depth seen by the probe as it traverses an atom sample of

length L with the coupling beam turned off (see supplementary material Notes, Sec. S1 D). The OD is defined by the product of L with the on-resonance probe absorption $\alpha_{\Omega_c=0}$ (see Eq. (7) above): $OD = L\alpha_{\Omega_c=0} = N\omega_p|\mu_{13}|^2L/(\epsilon_0c\hbar\gamma_{13})$. To take this attenuation into account, we amend Eq. (8) to

$$\Gamma_{\text{EIT}} = 2\left(\gamma_{12} + \frac{|\Omega_c|^2}{\gamma_{13}\sqrt{OD}}\right), \quad (9)$$

where the power-broadened term is identical to Eq. (5) in Ref. 5 and Eq. (2) in Ref. 19.

E. The refractive index and slow light

We now shift focus to the real refractive index n_r (Eq. (4)), plotted in Figs. 2(d) and 2(f). In particular, using Eq. (5), we find that a strong coupling field induces a positive slope in n_r within the narrow EIT window,

$$n_r \xrightarrow{\Delta_p \sim 0} 1 + \frac{N}{2\epsilon_0} \frac{|\mu_{13}|^2}{\hbar} \frac{\Delta_p}{|\Omega_c|^2}, \quad (10)$$

as depicted in Fig. 2(f). We see from Eq. (10) that, if we ensure that the coupling field satisfies the condition,

$$|\Omega_c|^2 \ll \frac{N|\mu_{13}|^2}{2\epsilon_0\hbar} \omega_p, \quad (11)$$

we may produce a steep positive gradient about $\Delta_p \sim 0$. The group velocity of light v_g is defined by the relation $v_g/c \equiv (n_r + \omega_p dn_r/d\omega_p)^{-1}$. A steep positive gradient, therefore, leads to a significantly reduced group velocity for the probe. Applying Eqs. (10) and (11), we have

$$\frac{v_g}{c} \approx |\Omega_c|^2 / \left(\frac{N|\mu_{13}|^2}{2\epsilon_0\hbar} \omega_p \right) \ll 1. \quad (12)$$

From the definition of the on-resonance optical depth OD above, and assuming that the power-broadened term in Eq. (9) is dominant, we may re-cast Eq. (12) as

$$\frac{v_g}{c} = \frac{\Gamma_{\text{EIT}}}{\sqrt{OD}} \frac{L}{c} \propto \frac{I}{N}, \quad (13)$$

where we have used Eq. (16). This means that, when going through the sample, the probe light is delayed by a time τ_d , given by²⁰

$$\tau_d = \frac{L}{v_g} \sim \frac{\sqrt{OD}}{\Gamma_{\text{EIT}}} \propto \frac{NL}{I}. \quad (14)$$

Thus, the narrower the EIT window, the larger the pulse-delay τ_d .²¹ See Ref. 22 and Sec. 4.1 of Ref. 5 for more accurate predictions of the maximum achievable τ_d , which are achieved by making detailed measurements of the EIT lineshape and contrast, and incorporating some of these empirical values into the theory.

We wish to clarify two issues that often confuse students. First, the dramatic changes in n_r near resonance do not much impact the *phase velocity* of light (c/n_r), because n_r never significantly departs from unity for a dilute vapor—this is clearly visible in Figs. 2(d) and 2(f). No physical significance

is ascribed to the phase velocity, so that the fact that n_r dips below unity, causing the phase velocity to exceed c , is no cause for alarm. Second, the definition of v_g above suggests that when $dn_r/d\omega$ is negative, as is the case near-resonance just outside the EIT window, the group velocity may, in principle, exceed the phase velocity and even c . However, outside the EIT window the absorption is high; thus, no signal is actually able to propagate faster than c .¹⁵

F. Stored light and EIT-based quantum memory

In effect, a pulse of probe light is slowed and stored in the sample for a time τ_d ,²⁰ and the medium then acts as a quantum memory where information can be stored. Notice that the pulse undergoes a dramatic spatial compression inside the sample: The front end slows down upon entry into the sample and propagates at v_g , even as the pulse-rear, which is still outside, propagates at c . The compression factor is given by $L_p/L_0 = v_g/c$ where L_p is the length of the compressed pulse inside the medium and L_0 is the free-space pulse length.²⁰

However, from Sec. IID it is clear that Eq. (14) and the subsequent discussion apply only to a probe pulse for which the frequency bandwidth τ_p^{-1} fits within the EIT linewidth Γ_{EIT} , i.e., for a pulse such that $\tau_p^{-1} \leq \Gamma_{\text{EIT}}$. In other words, if τ_p is so short that the probe bandwidth is broader than Γ_{EIT} , then the probe frequency components outside the transparency window suffer significant absorption, causing the pulse to become distorted. Substituting this condition in Eq. (14), we find²³

$$\tau_p^{-1} \tau_d \leq \sqrt{OD}. \quad (15)$$

This relation between the bandwidth of the probe pulse and the pulse delay is known as the “delay-bandwidth product,” which is a figure of merit for a storage/memory device, as it is a measure of how many probe pulses fit within the sample (without being absorbed to the extent that they undergo distortion).^{5,20} A drawback of EIT-based quantum memory is that, owing to the narrow bandwidth requirements of EIT, this product remains low, e.g., for our longest observed τ_d of 68 μs (see Fig. 9(b)) and $\tau_p = 170 \mu\text{s}$ (see Sec. IVE), the delay-bandwidth product is 0.4. In our experiments, $\sqrt{OD} \approx 5$ (see Sec. VII A), so Eq. (15) is satisfied. Our OD and delay-bandwidth product are comparable to previous values reported for EIT-based quantum memory in warm ⁸⁷Rb vapor.^{5,24}

III. THREE-LEVEL ATOMS: IMPLEMENTATION IN THE LAB

In the lab, Rubidium is a popular choice of alkali, owing to the ready availability of inexpensive single mode diode lasers at the resonance wavelength for transitions from the $5^2S_{1/2}$ ground state to the $5^2P_{1/2}$ excited state (D1-transition; 795 nm) or the $5^2P_{3/2}$ excited state (D2-transition; 780 nm). Figure 3 shows the hyperfine energy-level structure for both stable isotopes ⁸⁵Rb (nuclear spin $I = 5/2$) and ⁸⁷Rb ($I = 7/2$).²⁵

Our experiments are performed on the D1 transition ($5^2S_{1/2}, F_g = 2 \rightarrow 5^2P_{1/2}, F_e = 1$) in ⁸⁷Rb atoms. The hyperfine D1 transition for ⁸⁷Rb involves the $5^2S_{1/2}$ ground state and the $5^2P_{1/2}$ excited state, which are split by the interaction of the valence electron’s total angular momentum

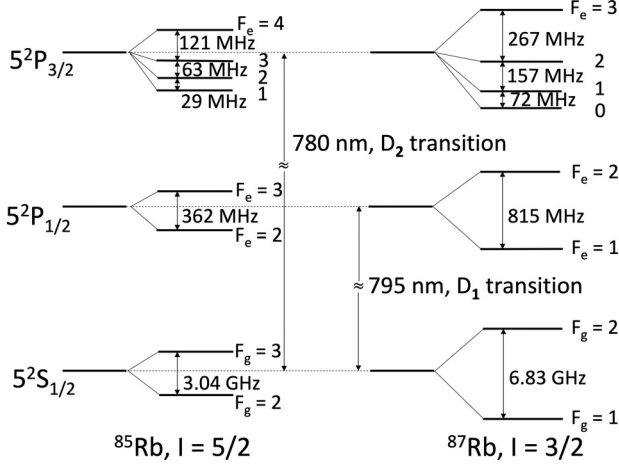


Fig. 3. Rb energy-levels with hyperfine structure.

(orbital + spin) with the nuclear spin, creating $F_g = 1, 2$ ground energy states (separated by 6.8 GHz), and $F_e = 1, 2$ excited energy states (separated by 815 MHz). Each hyperfine state F has $2F + 1$ degenerate substates with quantum number m_F ranging from $m_F = -F$ to F in increments of 1. Measurement will find the atom with an angular momentum component $m_F \hbar$ along a chosen quantization axis—we choose z as our axis of quantization. For the $F_g = 2$ ground state, for example, five magnetic substates are revealed in the presence of a weak external magnetic field B_z (along z) which lifts the degeneracy by imparting a Zeeman shift $\Delta E = g_f \mu_B m_F B_z$ to each magnetic sub-level. Here, g_f is the Lande g -factor for the hyperfine state ($g_f = 1/2$ for $F_g = 2$), μ_B is the Bohr magneton (9.274×10^{-24} J/T), and m_F is the magnetic sub-level number. The Zeeman shifts between the magnetic sub-levels of the $F_g = 2$ ground state are 7×10^9 Hz/T, resulting in a shift of 0.7 kHz when the field is 10^{-7} T (i.e., 1 mG).²⁵

A pump or probe laser tuned near-resonance to a particular $F_g \rightarrow F_e$ transition pumps other close-lying F_e states off-resonantly, creating extraneous channels for atomic population leakage, which diminishes the steady-state fraction of atoms in the dark state. The ^{87}Rb D1 transition is advantageous in that respect because the F_e level-separation of 815 MHz is largest, compared to that of the D1 transition in ^{85}Rb (362 MHz), and of the D2 transitions (Fig. 3). See Sec. IV C for further details.

A. Zeeman EIT: Spin polarization via optical pumping

Three-level schemes with alkali atoms for EIT-based slow light experiments fall into two categories: Hyperfine EIT and Zeeman EIT. Hyperfine EIT with ^{87}Rb is depicted in Fig. 4(a). A strong pump beam (coupling laser; solid line) is tuned to one $F_g \rightarrow F_e$ transition, while a weak beam (probe; dashed line) is tuned to the other transition, 6.83 GHz apart. The probe is created using an electro-optic modulator to split off a small amount of the coupling beam, or by using two phase-locked lasers, each tuned to either transition. Zeeman EIT, depicted in Fig. 4(b), is less resource-intensive, requiring a single passively-stable laser system and less expensive acousto-optical modulators. Hence, we confine our attention to this method. Zeeman EIT relies upon the optical pumping of the magnetic Zeeman sub-levels created by applying a weak external magnetic field B_z , using a strong coupling

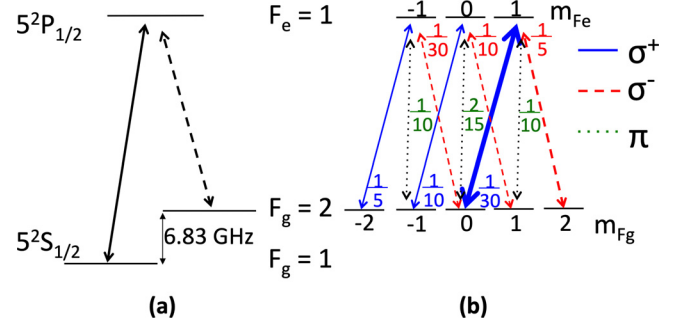


Fig. 4. Three-level lambda schemes for (a) hyperfine EIT and (b) Zeeman EIT. In (b), the transition strength between a pair of magnetic sub-states depends on both the light polarization and the magnetic quantum numbers of the two levels involved. The relative strengths are indicated for σ^+ (solid lines), σ^- (dashed lines), and linear (π ; dotted lines) polarizations of light (Ref. 25,26). The ground states $m_{F_g} = 2, 0$ and the excited state $m_{F_e} = 1$ approximate the three levels $|1\rangle, |2\rangle, |3\rangle$ in Fig. 1(a), respectively.

beam and a weak probe beam of mutually orthogonal circular-polarization (one beam σ^+ , the other σ^-). Both beams propagate collinearly with B_z .

Figure 4(b) depicts a strong σ^+ coupling field (solid arrows) and weak σ^- probe field (dashed arrows), tuned to near-resonance with the $(5^2S_{1/2}, F_g = 2) \rightarrow (5^2P_{1/2}, F_e = 1)$ transition.^{25,26} The dipole selection rules for transitions induced between magnetic substates by σ^+ (σ^-) light are $\Delta m = +1$ (-1) for absorption and $\Delta m = -1$ ($+1$) for stimulated emission, in addition to the $\Delta m = 0, \pm 1$ selection rule for spontaneous emission transitions.²⁵ This means that after many absorption–emission cycles have occurred, the strong σ^+ field optically pumps the atoms into the $m_{F_g} = 0$ sub-state. From here, the pump excites the atoms to the $m_{F_e} = 1$ sub-state, which is followed either by spontaneous decay to the $m_{F_g} = 1, 2$ spin sub-states (where they stay) or by emission back into the $m_{F_g} = 0$ state (in which case they are re-excited). Eventually, after a time that is long compared to the excited state lifetime of 27.7 ns for the Rb D1 line, the atoms accumulate into the $m_{F_g} = 1, 2$ spin sub-states (typically, after pumping on a time-scale of ms). The action of the weak σ^- probe is to optically pump some of these atoms toward lower m_{F_g} -states. Eventually, in the steady-state, the atomic population is concentrated in the $m_{F_g} = 0, 2$ spin sub-states. Thus, the atom is “spin-polarized” via optical pumping.²⁷

Indeed, the ideal three-level lambda system (states $|1\rangle, |2\rangle$, and $|3\rangle$ in Fig. 1) is well-approximated by the ground states $m_{F_g} = 2, 0$ and the excited state $m_{F_e} = 1$. In Fig. 4(b), the pump (thick solid arrow) and probe (rightmost dashed arrow) are highlighted. The method for fine-tuning the pump and probe laser frequencies to resonance with these particular Zeeman sub-levels is described in Sec. IV C. These approximate three-level atoms then evolve into the dark state, enabling EIT and slow light. Factors causing spin relaxation that reduce the dark state population are discussed in Sec. III B below.

Note that the assumption made at the beginning of Sec. II, that the coupling beam only addresses levels $|2\rangle$ and $|3\rangle$, and the probe beam only addresses levels $|1\rangle$ and $|3\rangle$, is automatically satisfied in Zeeman EIT because σ^+ pump photons cannot be absorbed by the $|m_{F_g} = 2\rangle \rightarrow |m_{F_e} = 1\rangle$ transition and σ^- probe photons cannot be absorbed by the $|m_{F_g} = 0\rangle \rightarrow |m_{F_e} = 1\rangle$ transition. The assumption is also satisfied in

the case of hyperfine EIT, where the 6.83 GHz difference between the pump and probe frequencies in Fig. 4(a) is large enough that the pump beam experiences negligible absorption on the probe transition, and vice versa.

B. Spin relaxation mechanisms: Role of buffer gas

There are several spin-depolarization mechanisms that reduce the EIT contrast and affect its linewidth. The spin-polarized Rb atoms prepared in the previous subsection exist within the sample volume that is jointly illuminated by the pump and probe beams. Typically, in a glass cell filled with warm alkali vapor, this volume is the central part of the cell. However, the atoms are moving at thermal speeds, so that the polarized atoms can exit the illuminated volume. Collisions with the glass wall destroy the atoms' polarization,²⁸ and these unpolarized atoms may subsequently re-enter the illuminated region. These transit-time effects reduce the sample polarization.²⁹ Further, there are spin-exchange collisions between spin-polarized Rb atoms which can redistribute the populations in the magnetic sub-states, causing depolarization.²⁸

There are two commonly used approaches to suppress the spin-depolarizing effects described above:²⁷ (i) include an inert buffer gas such as Ne, He, or Ar in the Rb vapor cell or (ii) coat the inside of the glass vapor cell with an anti-relaxation coating such as paraffin.

Coated cells can yield significantly longer spin coherence times than buffer gas cells because the paraffin coating suppresses the Rb spin-depolarization via “softer” atom-wall collisions. However, the light-Rb atom interaction dynamics in coated cells is more complicated, yielding a dual-structured EIT lineshape with a narrow central peak sitting atop a broad pedestal (see, for example, Ref. 5 and references therein). The broad pedestal is due to Rb atoms interacting with light during a one-time pass through the light beams. The narrow peak, on the other hand, results from contributions by polarized Rb atoms that transit in and out repeatedly through the laser beams, interacting coherently each time with the pump and probe fields. These atoms have many wall collisions before eventually becoming depolarized. The linewidth of the narrow peak is significantly affected by factors such as coating quality and cell geometry.⁵ These effects tend to make the EIT data more difficult to interpret so that, in the work reported here, we do not use coated cells.

In buffer gas cells, the usual practice for EIT and slow light experiments is to mix noble gas (up to several tens of Torr) with a few microTorr of Rb.⁵ In our experiments, we use 10 Torr of Ne. Frequent Rb–Ne collisions reduce the Rb atoms' mean free path to values much smaller than the pump beam diameter,³⁰ thus confining the atoms within the illuminated volume. Instead of flying through the laser beam at thermal speeds, the atoms then slowly diffuse through, thereby increasing the laser-atom interaction time by several orders of magnitude.⁵ Note that Rb–Ne collisions cause the spin-polarized Rb atom's velocity to change, but with negligible spin relaxation. Such collisions that rapidly redistribute the atomic velocities without re-equilibrating the populations of the atomic levels are termed “velocity-changing collisions” in the literature.^{27,30} At the considered partial pressures, Rb–Rb and Rb-wall collisions are negligible compared to Rb–Ne collisions.

Still, decoherence effects remain that are not addressed by the buffer gas (or by wall coatings). Inhomogeneities in the magnetic field used for Zeeman EIT cause spatial variation of the dark state leading to absorption. In Sec. S2 of the supplementary material,¹¹ we discuss how to suppress these inhomogeneities. Furthermore, an incoherent pumping mechanism, known as radiation trapping, may become significant at high atomic densities. Radiation trapping refers to the reabsorption of spontaneously emitted photons within the illuminated volume, and is expected to become significant inside our probe beam radius at number densities $N \geq 5 \times 10^{11} \text{ cm}^{-3}$ (see Sec. IV D).³¹ Hence, we keep our number density below this value (see Secs. V and S2 D).

C. Slow light conditions; estimate of γ_{12} , γ_{13}

Let us examine how the conditions for slow light, Eq. (5) and Eq. (11), are satisfied in our experiments. The relation between the Rabi frequency Ω_c and coupling beam intensity I , in the case of the spin-polarized atom in Fig. 4(b), is defined through the well-known expression for the saturation intensity I_{sat} ,^{18,25,32}

$$\frac{(2|\Omega_c|)^2}{\Gamma^2} \equiv \frac{I}{2I_{\text{sat}}}, \quad \text{where } I_{\text{sat}} = \frac{\pi\hbar c}{3\lambda^3} \Gamma. \quad (16)$$

Here, λ is the optical wavelength for the transition, and Γ is the natural linewidth due to spontaneous emission.²⁵ I_{sat} is the excitation intensity at which the stimulated emission rate is half the spontaneous emission rate. For the ⁸⁷Rb D1 transition, $\Gamma = 2\pi(5.75 \text{ MHz})$ and $\lambda = 794.98 \text{ nm}$ ($\omega_p/2\pi = 3.77 \times 10^{14} \text{ Hz}$), yielding $I_{\text{sat}} = 1.5 \text{ mW/cm}^2$.²⁵ Our pump intensity I mostly varies between 1.25 and 5.6 mW/cm^2 (see Sec. IV D), which means $|\Omega_c|/2\pi$ ranges from 1.9 to 3.9 MHz.

The ground state decoherence rate γ_{12} arises from Rb–Rb collisions, Rb collisions with the cell walls, and from Rb atoms eventually diffusing out of the illuminated volume despite the buffer gas. Collisions with the inert buffer gas do not contribute significantly to γ_{12} . However, since our experiments use Zeeman hyperfine levels, inhomogeneities in the magnetic field contribute to γ_{12} . Good suppression of stray magnetic fields (Sec. S2, supplementary material)¹¹ results in a value $\gamma_{12} \approx 3 \text{ kHz}$, as reported in the literature.^{33,34} Clearly, $\Omega_c \gg \gamma_{12}$, and since $\Delta_p/2\pi \sim 100 \text{ kHz}$ or less (see Figs. 2(e) and 2(f) and 8) our experiments fall in the strong coupling intensity regime, i.e., the condition in Eq. (5) is well-satisfied.

Next, to check that Eq. (11) is also well-satisfied in our experiments, we note that the dipole matrix element $|\mu_{13}|$ for the ⁸⁷Rb D1 transition in our spin-polarized atom is well-approximated by just the magnetic quantum number-independent value (known as the reduced matrix element) $2.54 \times 10^{-29} \text{ cm}$.²⁵ The number density N is $\sim 1.5\text{--}3.4 \times 10^{11} \text{ cm}^{-3}$ (see Sec. V), yielding $(1/2\pi)\sqrt{N|\mu_{13}|^2\omega_p/(2\epsilon_0\hbar)} \approx 2\text{--}4 \text{ GHz}$, which exceeds the $|\Omega_c|/2\pi$ -values by three orders of magnitude.

Finally, we estimate the excited state damping γ_{13} which arises from the spontaneous emission rate Γ , the dephasing γ_{coll} due to Rb collisions with the buffer gas, and the Doppler broadening Γ_D . Recall from Eq. (1) and Fig. 2(a) that γ_{13} is manifested as the half-width of the absorption peak. Our sample consists of a few μTorr of isotopically enriched dilute ⁸⁷Rb vapor mixed with 10 Torr of Ne buffer gas.

To estimate γ_{coll} we follow the empirical relation $2\gamma_{\text{coll}}/2\pi = 9.84 \text{ MHz/Torr}$ derived in Ref. 35. We see that, for 10 Torr of Ne, $\gamma_{\text{coll}}/2\pi \sim 50 \text{ MHz}$. On the other hand, the Doppler broadening of the absorption profile of Rb vapor, illuminated by a frequency-scanning monochromatic beam, arises due to the thermal motion of the atoms.³⁶ In a simple 1D situation, an atom moving with thermal velocity v_{th} toward or away from a laser beam of frequency ω_0 sees a Doppler-shifted frequency $\omega_0(1 \pm v_{\text{th}}/c)$. This means that for a thermal distribution of velocities we may estimate the full width at half maximum (FWHM), Γ_D , of the Doppler broadened absorption profile to be $\Gamma_D = 2\omega_0 v_{\text{th}}/c = 2k v_{\text{th}}$. Here, $k = 2\pi/\lambda$ is the magnitude of the incident field wave vector. If we use the most probable velocity $v_{\text{th}} = \sqrt{(2 \ln 2) k_B T/m}$, we obtain $v_{\text{th}} \approx 200 \text{ m/s}$ at $T = 293 \text{ K}$, yielding $\Gamma_D/2 \approx 2\pi(250 \text{ MHz})$ at $\lambda = 795 \text{ nm}$. Thus, γ_{13} is dominated by γ_{coll} and $\Gamma_D/2$ (both are significantly larger than Γ). We use their sum as an estimate for γ_{13} .

Note from Eqs. (9) and (13), that, in the high coupling intensity limit, both v_g and Γ_{EIT} decrease linearly with the intensity. However, lowering the intensity too far (although still in the high intensity limit) may reduce the steady-state population in the dark state enough that slow light effects start to degrade, causing the probe pulse to distort and appear to speed up again. Thus, we may expect a sweet spot in the pump intensity, where conditions for slow light are optimized (see Sec. VII C).

IV. EXPERIMENTAL SETUP

In this section, we describe how we create pump, probe, and reference beams, tuned to the appropriate alkali transitions for Zeeman EIT shown in Fig. 4(b), and of the required size, intensity, frequency, temporal width, and polarization purity. Our optical layout is depicted in Fig. 5.

A. Laser source

We use a commercial external cavity tunable diode laser (ECDL) to provide linearly polarized continuous-wave light at $\sim 795 \text{ nm}$. A few percent of the output is split off for use in a saturated absorption spectroscopy (SAS) set-up to enable the precise tuning of the laser to the $F_g = 2 \rightarrow F_e = 1$ D1 transition, as described below.

The main ECDL output is first passed through a Faraday rotation-based optical isolator (OI) which optically isolates the laser from back reflections (e.g., arising from the optics that couple the light into the fiber). The light then passes through an anamorphic prism pair to circularize the elliptical cross-section of the beam, before coupling into a single-mode polarization-maintaining fiber which preserves the direction of the linear polarization of the input beam (we measured a residual drift of $<2\%$ in the polarization direction at the fiber output). The single-mode fiber is typically aligned and operated at a transmission efficiency of only 30%–50%, but produces a clean Gaussian spatial profile. Gaussian spatial profiles are highly desirable for pump-probe experiments where the pump and probe beams must be well-collimated, and must have good spatial overlap that is amenable to quantitative modeling.

B. Creating the pump and frequency-scannable probe

The output from the fiber ($\sim 7 \text{ mW}$) is collimated using an aspheric lens. The collimated light is divided by a polarizing beamsplitter (PBS 1) into two orthogonally linearly polarized beams—the strong coupling (or pump) beam (solid line) and weak probe beam (dashed line).

In pump-probe spectroscopy, the probe is swept in frequency around the fixed pump frequency, and the probe transmission spectrum is detected. The sweeping is accomplished with an acousto-optic modulator (AOM), which is a device that uses a sound wave propagating through a crystal to form a diffraction grating for incoming light waves, producing frequency-upshifted (+1) and downshifted (−1) orders, in addition to the 0 order at the incident frequency.^{17,37} The ± 1 orders emanate at a slight angle to the direction of the incident beam, symmetrically on either side, while the 0 order continues along the incident beam direction. By carefully aligning the angle of incidence of the beam on the AOM, we achieve about 70% of the incident power in the first order of choice, with most of the remaining power in the 0 order, while a small amount leaks into the undesired first order. The AOM performs a frequency-scan by introducing a fixed offset (80 MHz in our case) and sweeping back and forth about that fixed offset value by some desired amount (chosen by the user to be any value from zero up to a maximum sweep $\pm 20 \text{ MHz}$ for our AOM).

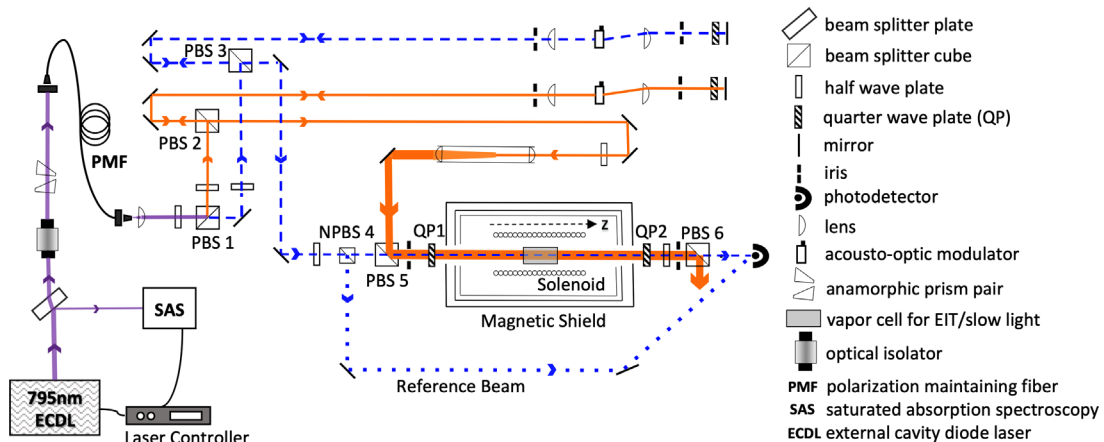


Fig. 5. Optical setup. The laser is split at a polarizing beamsplitter (PBS 1) into a strong pump, or coupling, beam (solid lines) and a weak probe beam (dashed lines). Before entering the vapor cell, the probe beam is split at a non-polarizing beamsplitter (NPBS 4) to create a reference beam (dotted lines) for the slow light measurement. A Zeeman splitting magnetic field is created within the vapor cell, along the indicated z axis.

For the purpose of measuring the EIT linewidth in Figs. 2(c) and 2(e), a sweep of ± 100 kHz suffices (see Fig. 8). Because of the fixed frequency-offset of 80 MHz that the AOM introduces, we must insert an identically configured AOM in the path of the pump beam as well, so that both the pump and probe beams are offset in frequency by the same amount. To drive the AOMs, a dual-output waveform generator which creates twin phase-locked identical 80 MHz 1 V signals is used. Each signal is amplified using a standard RF amplifier before being fed to the AOM. Planoconvex lenses of focal length 30 cm are placed on either side of each AOM, with the AOM crystal located at the common focal spot.

One problem we encountered is that the angle of the diffracted orders changes when the output frequency is varied, causing a spatial shift in the beam at the vapor cell located a few feet downstream. This shift is a problem because the probe beam moves off the center of the vapor cell during the course of its frequency scan. To overcome this problem, the desired diffracted order is retroreflected back through the crystal (see top right hand corner of Fig. 5), such that the double-shifted order is aligned with the incident beam but in the counter-propagating direction.³⁷ For this double-shifted beam the angular deflection from the second pass cancels the deflection from the first pass. The cancellation is not ideal, due to unavoidable imperfections in alignment, but the spatial shifting of the scanning probe at the site of the vapor cell is highly suppressed in this double-pass AOM configuration. The presence of the quarter waveplate just before the retroreflecting mirror in Fig. 5 serves to orthogonally polarize the double-shifted order with respect to the incident beam, enabling the separation of the double-passed and incident beams at a polarizing beamsplitter (PBS 2 for the pump, PBS 3 for the probe).

C. Frequency tuning pump and probe to EIT window

The frequency-tuning of the laser for implementing Zeeman EIT is achieved in two steps. First, the laser is tuned to the $5^2S_{1/2}, F_g = 2 \rightarrow 5^2P_{1/2}, F_e = 1$ ^{87}Rb D1 transition, using the method of saturated absorption spectroscopy (SAS). Next, the pump and probe beams are fine-tuned to the $m_{F_g} = 2, 0$ and $m_{F_e} = 1$ Zeeman sub-levels with the AOMs (see Fig. 4(b)).

SAS is performed in a second vapor cell, that is not explicitly shown in Fig. 5. This cell is at room temperature, is filled with natural abundance Rb vapor (72% ^{85}Rb , 28% ^{87}Rb), has no buffer gas, and the walls are uncoated. Figure 6 shows the transmission spectrum of a weak beam diverted from the ECDL into the SAS cell, where the D1 transitions for the two Rb isotopes are displayed in one continuous scan. In plot (a), the Doppler-broadened D1 transitions are shown, before SAS is performed. Only for the ^{87}Rb D1 F_e states do the level separation of 815 MHz exceed the Doppler broadening $\Gamma_D/2\pi$ for Rb vapor (see Sec. III C), enabling the two excited states to be resolved. The ^{85}Rb D1 transitions, with their smaller F_e separations, are totally smeared out by Doppler broadening. However, when SAS is performed, by introducing in the cell a strong beam that is spatially overlapping with the weak beam but counter-propagates, the absorption is saturated for the velocity-class of atoms that travels in a direction perpendicular to both the strong and weak beams. The hyperfine transitions are revealed as narrow ‘‘holes’’ that are ‘‘burnt’’ into the Doppler-broadened absorption spectra—these holes are manifested as ‘‘bumps’’ in the transmission spectrum in Fig. 6(b). In plot (c), the Doppler component is

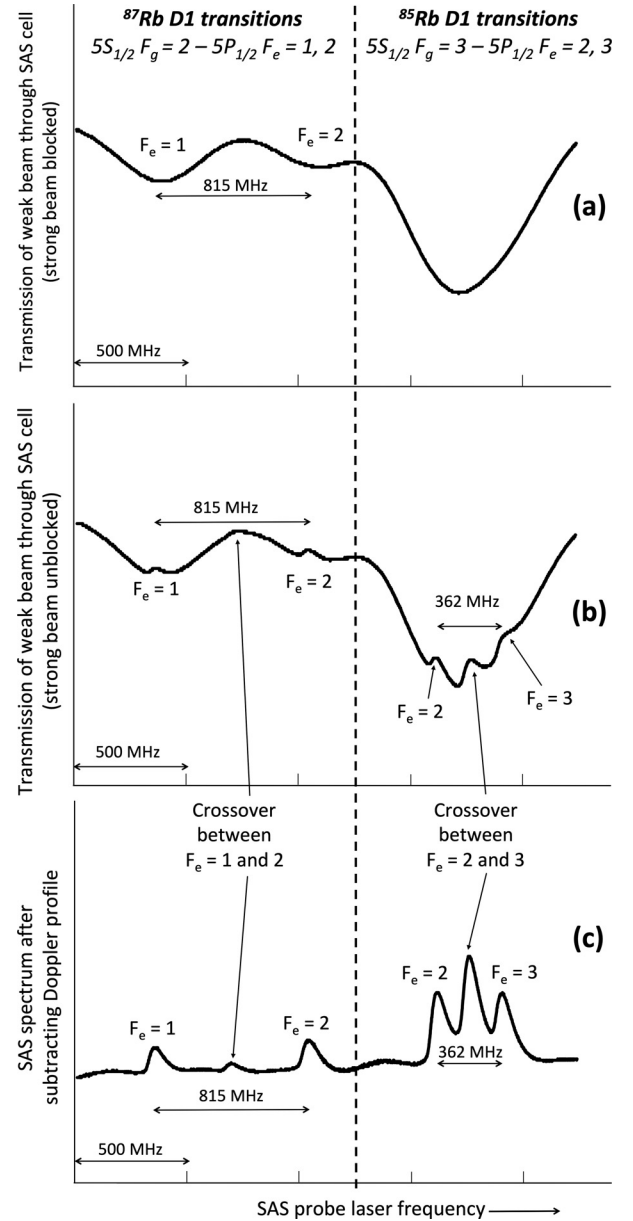


Fig. 6. Tuning the ECDL to the $5^2S_{1/2}, F_g = 2 \rightarrow 5^2P_{1/2}, F_e = 1$ ^{87}Rb D1 transition via saturated absorption spectroscopy. (a) Transmission spectrum for a weak beam propagating through a Rb vapor cell with uncoated walls and no buffer gas (placed inside the box marked SAS in Fig. 5). The Doppler broadened D1 transitions in ^{85}Rb and ^{87}Rb are displayed in one continuous scan. The $F_e = 2$ and 3 transitions in ^{85}Rb are obscured, but the $F_e = 1$ and 2 transitions in ^{87}Rb are resolved owing to their large separation of 815 MHz. (b) A strong counter-propagating beam is introduced, revealing the hyperfine structure, even more clearly in (c) by subtracting away the Doppler component and magnifying the vertical scale (Ref. 38).

subtracted away and the vertical scale is magnified. The laser is tuned to the $F_e = 2 \rightarrow F_e = 1$ ^{87}Rb D1 peak in plot (c) by reducing the scan to zero, while staying centered on this particular feature, and the goal of SAS is achieved. Note that atoms that have a velocity component, say, along one of the laser beams, may be down-shifted into resonance with that beam on a particular D1 transition, while being simultaneously up-shifted into resonance with the counter-propagating beam on the higher adjacent D1 transition—this results in ‘‘crossover’’ peaks midway between adjacent D1 transitions. See Ref. 38 for further details on SAS.

In order to obtain EIT transmission spectra, such as those shown in Fig. 8, the frequencies of the pump and probe beams need to be further fine-tuned into resonance with the Zeeman sub-levels $m_{F_g} = 0 \rightarrow m_{F_e} = 1$ and $m_{F_g} = 2 \rightarrow m_{F_e} = 1$, respectively (see Fig. 4(b)). This fine-tuning is achieved inside the magnetically shielded vapor cell in Fig. 5 described in Secs. III B and III C. The magnetic field B_z for Zeeman splitting is created by a solenoid. Details on the Rb–Ne vapor cell are provided in Sec. V. Details on the magnetic shielding and solenoid are given in Sec. S2 of the supplementary material.¹¹ Note that we must take into account the Zeeman shifts of 0.7 kHz/mG between the magnetic sub-levels of the $F_g = 2$ ground state.²⁵ In our experiments, $B_z = 50$ mG, yielding a Zeeman splitting between adjacent ground sub-states of 35 kHz. Because the SAS procedure tunes the ECDL frequency before the laser is split into pump and probe, this means that if the pump happens to be in resonance with the $m_{F_g} = 0 \rightarrow m_{F_e} = 1$ transition, the probe (which is at the same frequency) is detuned from the $m_{F_g} = 2 \rightarrow m_{F_e} = 1$ probe transition by $\Delta_p = 70$ kHz (position A in Fig. 7). Scanning the probe AOM frequency (A \leftrightarrow C) symmetrically about position B in Fig. 7, where the probe detuning $\Delta_p = 0$ (or more precisely, where the two-photon detuning is zero; see Sec. II D), yields EIT resonance spectra as displayed in Fig. 8. For the slow light experiments, the scan is reduced to zero while staying centered at B.

It is worth noting that, before the strong (co-propagating) pump is turned on, the weak probe experiences an absorption profile in the Rb–Ne vapor cell that resembles Fig. 6(a). In Sec. III C we estimated the linewidth γ_{13} , arising from Doppler and collisional broadening in the Rb–Ne cell, for the D1 transitions to be comparable to those shown in Fig. 6(a). Turning on the strong co-propagating pump activates the narrow EIT window predicted by Fig. 2(b), and observed in Fig. 8. It is clear from Fig. 6(a) that even though the $F_g = 2 \rightarrow F_e = 1$ ^{87}Rb D1 transition is advantageous for slow light experiments because this particular transition has the least spectral overlap with neighboring D1 transitions, some residual overlap of the $F_e = 1, 2$ levels is visible. This suggests it is likely there is leakage of atoms from the $F_e = 1$ to the $F_e = 2$ level in the Rb–Ne vapor cell, resulting in a diminished dark state population and a reduced EIT contrast.

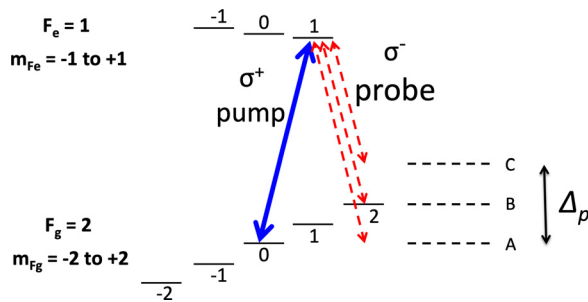


Fig. 7. Fine-tuning the pump and probe laser frequencies to the $m_{F_g} = 0 \rightarrow m_{F_e} = 1$ and $m_{F_g} = 2 \rightarrow m_{F_e} = 1$ sub-levels, respectively. Tuning the ECDL via SAS may put the pump in resonance with the pump transition but leaves the probe, which is at the same frequency, detuned from the probe transition by $\Delta_p = 70$ kHz (position A). EIT resonance is achieved by fine-tuning the probe frequency with the probe AOM so that Δ_p is reduced to zero (position B). Scanning the probe frequency symmetrically about B generates the EIT spectra, such as those shown in Fig. 8.

D. Pump and probe beam size and pump intensity

The probe beam is Gaussian with a $1/e^2$ -radius of 1.13 mm (the distance from the center of the beam where the intensity drops to $1/e^2$ of its value at the center). To approximate an ideal plane wave (see Sec. 1 in supplementary material Notes), the pump beam, which is also Gaussian, is expanded to a $1/e^2$ -radius of 2.26 mm using a telescope comprising two simple plano-convex lenses mounted in a cage assembly (see Fig. 5). The pump intensity was mostly varied between 1.25 and 5.6 mW/cm².

E. Probe and reference pulses and probe intensity

In our experiments, the probe beam is in the form of a short (temporal) Gaussian pulse. Slow light demonstrations consist of measurements of the delay of the probe pulse propagating through the sample, relative to an identical reference pulse propagating along a similar path-length outside the sample. This reference pulse, depicted by the dotted lines in Fig. 5, is split off from the probe pulse by inserting a non-polarizing beamsplitter NPBS 4 into the probe path, as shown. The probe and reference pulses are created by amplitude modulation of the probe AOM: The probe RF amplifier output is pulsed on and off by pulsing the input from its waveform generator. It is then straight-forward to measure time-delays between the centers of temporal Gaussian pulses. The pulse repetition rate is chosen so that the spacing between consecutive probe pulses far exceeds the achievable time-delay between a probe–reference pulse pair. These delays are typically tens of μs (see Sec. VII). Thus, we set the time period for the amplitude modulation of the probe AOM at a few ms (3.4 ms in our case).

Matching the reference pulse path-length to the probe path is a loose requirement because light takes only about a nanosecond to travel 30 cm in air—which is negligible compared to the delay induced by the slowing down of the light in our experiment. The reference and probe pulses are made incident on the same photodetector, and the delay in their arrival times is measured on an oscilloscope by blocking one pulse (with a card) while detecting the other.

From Sec. II F, the durations of the Gaussian probe and reference pulses must be long enough that the pulse frequency-bandwidth (estimated as the inverse of the $1/e$ -pulse-duration τ_p) fits inside the EIT spectral window Γ_{EIT} . According to Eq. (9) the EIT linewidth broadens linearly with pump intensity, necessitating probe pulses of progressively longer duration as the pump intensity decreases. For convenience, we keep the probe pulse duration constant, and long enough so that the frequency bandwidth fits inside the EIT linewidth for the full range of pump intensities (see Secs. VI and VII B).

The probe intensity must be kept significantly less than the pump, in order to satisfy the weak probe assumption. However, the probe pulse is too short to register on a typical power meter. Therefore, we illuminated a fast photodiode with continuous-wave light of known intensity, and calibrated the response in volts (as measured on an oscilloscope) per mW. Next, the probe pulse was shone upon the diode and the shape of the voltage response recorded. In our case the pulses have a $1/e$ -width of 170 μs , and the peak of the probe Gaussian temporal waveform is set at 0.3 mW/cm² (the average intensity of the probe pulse is 0.12 mW/cm²).

F. Leakage of pump beam into the detected probe mode

The pump and probe beams are recombined at polarizing beamsplitter PBS 5, so that the pump is reflected while the probe is transmitted toward the Rb–Ne vapor cell. A half-wave plate, placed in each beam before PBS 5, adjusts the relative intensity of the pump and probe beams. Because of the large pump beam size, the corresponding half-wave plate (10 mm diameter) is located before the beam expander. PBS 5 has the property that 99.5% of s -polarization (light polarization normal to plane of incidence) is reflected whereas only 90% of p -polarized light (light polarization parallel to plane of incidence) is transmitted. In our setup, s is vertical polarization (perpendicular to the optics table surface) and p is horizontal (parallel to the table surface). For this reason, the pump beam, which must be strong, is chosen to be s -polarized, and the probe is p -polarized.

The combined beams, which are orthogonal-linearly-polarized, are passed through a quarter-wave plate (QP 1 in Fig. 5) and converted to orthogonal-circularly-polarized before entering the vapor cell, as is required for the Zeeman EIT Λ -scheme. Irises are inserted to assist in day-to-day alignments. A second quarter-wave plate (QP 2) placed after the vapor cell converts the σ^+ and σ^- polarizations back to linear polarization so that the pump can be separated from the probe at a polarizing beamsplitter (PBS 6). A half-wave plate placed just after QP 2 is adjusted so that the probe transmits through PBS 6 and is focused onto a photodiode, while the pump is reflected away. The probe transmission spectrum is recorded via a fast photodiode connected to a digital oscilloscope. The impedance of the detector is kept low ($10\text{ k}\Omega$) in order to reduce electrical reflections in the BNC cable between the detector and oscilloscope, at the cost of reduced overall voltage signal.

It is obviously important to suppress as much as possible leakage of the strong pump beam into the detector at polarizing beamsplitter PBS 6. Polarizing beamsplitter cubes typically provide an extinction of $10^5:1$. For the highest pump powers used in our experiment, we found that a 0.1% pump leakage at PBS 6 more than doubles the power in the detected probe mode. Further, pump leakage may distort the shape of the probe pulse because the pump-profile is not entirely flat. A cleaner probe signal is obtained by the use of a Glan–Thompson polarizer (extinction ratio $10^5:1$) as PBS 6 for pump-probe separation. Despite careful attempts to minimize the pump light from leaking into the probe detector, we observed some residual pump leakage. We suspect this is due to the use of low-order wave plates (as opposed to more expensive zero-order wave plates) and to residual errors in the alignment of QP1 and QP2’s optical axes.

V. MAGNETICALLY SHIELDED WARM VAPOR CELL

For our slow light experiments, we use a pyrex glass vapor cell, that is a sealed cylinder of 25 mm diameter, containing a small amount of isotopically pure solid ^{87}Rb metal, along with 10 Torr of Ne buffer gas. Heating the cell is a convenient way to controllably vary the Rb atomic concentration in the vapor phase, yielding a few μTorr of ^{87}Rb vapor. A heater assembly is used to vary the cell temperature from 55 to 65°C during the experiment, thus varying the Rb atomic number density N participating in EIT between 1.5×10^{11} and $3.4 \times 10^{11}\text{ cm}^{-3}$ (see the supplementary material, Sec.

S2).¹¹ The length of the cell (28 mm) includes 1.6 mm windows (not anti-reflection coated) on either end. Therefore, the length of the vapor sample L is taken to be 25 mm. The cell is placed inside a solenoid as shown in Fig. 5. To enable Zeeman EIT, the solenoid applies a small magnetic field $B_z = 50\text{ mG}$, co-linear with the laser beam propagation. The cell, solenoid, and heater assembly are placed inside a magnetic shield in order to reduce stray magnetic fields incident on the sample below 0.2 mG, i.e., $< 0.5\%$ of B_z (see the supplementary material, Sec. S2).¹¹

VI. SETTING THE PROBE PULSE BANDWIDTH

In order to observe slow light, we need to ensure that the probe (and reference) pulse bandwidth is less than the EIT spectral window Γ_{EIT} . The EIT spectrum is obtained by the procedure described in Sec. IV C.

Figure 8 shows EIT lineshapes (and in the inset, EIT linewidths) obtained by measuring the probe transmitted power as a function of the probe detuning Δ_p for pump intensities ranging from 1.3 to 5.5 mW/cm^2 , which correspond to $\Omega_c/2\pi$ -values of 1.9 and 3.9 MHz , respectively (see Sec. III C). The maximum contrast measured (for the highest intensity of 5.5 mW/cm^2) is only $\sim 25\%$, for reasons explained in Secs. II D and III B; the contrast decreases as the pump intensity is lowered. In order to enable a visual linewidth comparison between the lineshapes obtained at different pump intensities, we normalized the lineshapes and displayed them on the same vertical scale, as is shown for (a) the highest and (b) the lowest intensities. We fit each lineshape to a Lorentzian (thin black curves), for which the FWHM yields the value for $\Gamma_{\text{EIT}}/2\pi$. In the inset, the data-points represent EIT linewidths extracted from these fits for five different pump intensities, and the line represents the prediction for $\Gamma_{\text{EIT}}/2\pi$ from Eq. (9). We note that a close look at the zero probe detuning point in the main figure reveals that the data are spectrally narrower at the center of the Lorentzian owing to coherent contributions from atoms that diffuse in and out of the laser beam multiple times without decohering (this is known as Ramsey-narrowing).^{5,33}

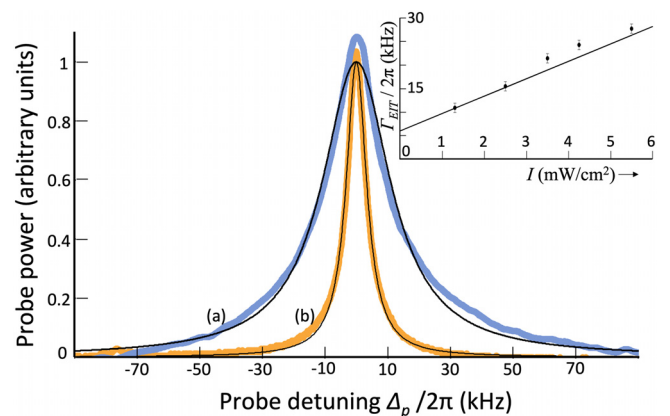


Fig. 8. Typical EIT lineshapes (probe transmitted power versus probe detuning) measured in a few μTorr of isotopically pure ^{87}Rb vapor with 10 Torr Ne at 65°C , for pump intensities of (a) $I = 5.5\text{ mW/cm}^2$ ($\Omega_c/2\pi = 3.9\text{ MHz}$) and (b) 1.3 mW/cm^2 ($\Omega_c/2\pi = 1.9\text{ MHz}$). The figure shows normalized EIT lineshapes, measured for the highest (blue line) and lowest (orange line) pump intensities, to allow a visual comparison of the linewidths. The Lorentzian fits (thin black curves) are included. The inset shows good agreement between the observed EIT linewidths (data points), and $\Gamma_{\text{EIT}}/2\pi$ predicted by Eq. (9) (line), for five different pump intensities.

We chose a $1/e$ -width of $170 \mu\text{s}$ for our Gaussian probe and reference pulses (see Sec. IV E). The corresponding bandwidth of $\leq 1 \text{ kHz}$ fits inside the EIT window, which, from Eq. (9), is at least $2\gamma_{12}/2\pi \approx 6 \text{ kHz}$ wide even for the smallest pump intensities.

Generating a EIT lineshape measurement as in Fig. 8 typically takes 40 ms for the higher pump intensities, and 160 ms for the lower intensities (we set the AOM for a $\pm 100 \text{ kHz}$ frequency-sweep in 10 ms; each spectrum in Fig. 8 is an average of either 4 or 16 such sweeps). Our laser system's passive stabilization yields a frequency drift of $< 10 \text{ MHz/h}$, resulting in a drift of less than 0.5 kHz while generating these EIT data-profiles.

VII. RESULTS AND DISCUSSION

In order to create short pulses, the probe frequency scan is now turned off, the probe AOM offset voltage is tuned to the EIT peak, and the amplitude modulation is turned on, as described in Sec. IV E. Once both slow and reference pulses are detected on an oscilloscope, the temporal waveform for each is fit to a Gaussian curve, and the relative delay time τ_d is extracted. Typical measurements of τ_d are presented in

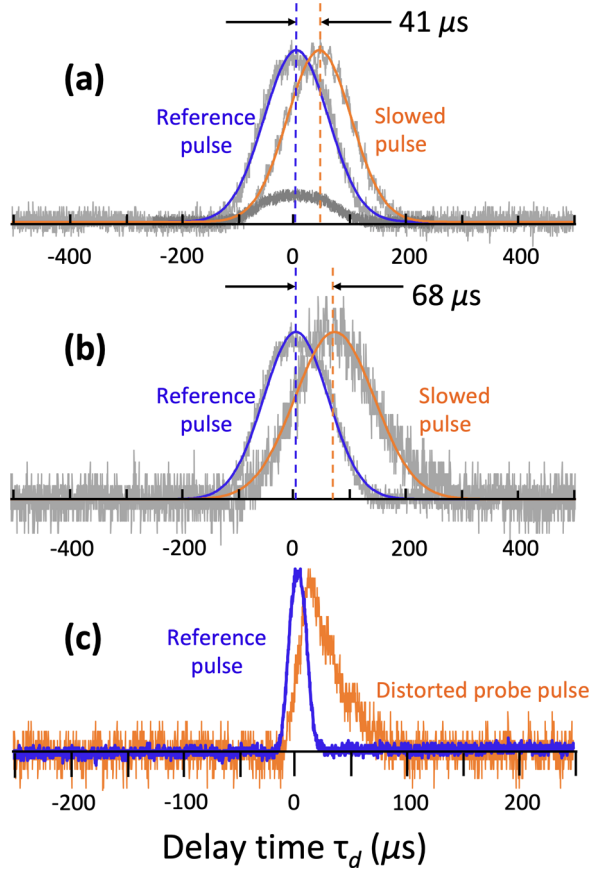


Fig. 9. Measurement of time-delay τ_d between reference and probe pulses traveling through air and the EIT medium, respectively. (a) $\tau_d = 41 \mu\text{s}$ yields $v_g = 610 \text{ m/s}$. Pump intensity $I = 3 \text{ mW/cm}^2$. The squat data-curve is the transmitted probe pulse when the pump is blocked, in which case EIT ceases so that large absorption occurs with no slowing. (b) $\tau_d = 68 \mu\text{s}$ yields $v_g = 368 \text{ m/s}$, our slowest observed velocity. Pump intensity $I = 1.2 \text{ mW/cm}^2$. (c) Significant distortion in the transmitted probe pulse occurs if we select a pulse duration so narrow that the probe bandwidth does not fit inside the EIT transparency window. All measurements are in ^{87}Rb vapor with 10 Torr Ne at 65°C .

Fig. 9, where the data (fuzzy lines) are shown along with Gaussian fits (smooth lines).

In Figs. 9(a) and 9(b), the reference pulse arrives at the detector earlier than the probe by $\tau_d = 41$ and $68 \mu\text{s}$, respectively, which corresponds to a slowed probe group velocity v_g of 610 and 368 m/s (using $v_g = L/\tau_d$). In each case, the peaks of the fits for reference and probe are scaled to the same value for easier comparison. The reference and probe pulse intensities are similar at the non-polarizing beamsplitter (NPBS4, Fig. 5), but the probe pulse suffers some absorption in the vapor (recall that our EIT contrast never exceeds 25%), which explains the increased noise on the slowed pulses. The slower group velocity was achieved by lowering the pump intensity which further reduces the overall signal-to-noise ratio.

A. Observed Γ_{EIT} , τ_d , and v_g versus theoretical prediction

To predict the EIT linewidth Γ_{EIT} , we insert in Eq. (9) parameter values that are relevant to our experiment, as discussed in Sec. III C: $\gamma_{12}/2\pi \approx 3 \text{ kHz}$, $\gamma_{13}/2\pi \approx 300 \text{ MHz}$. The optical depth is estimated using $N = 3.4 \times 10^{11} \text{ cm}^{-3}$ and $L = 2.5 \text{ cm}$ (see Sec. V), yielding $OD \approx 25$. The inset in Fig. 8 shows that the datapoints for $\Gamma_{\text{EIT}}/2\pi$ are in reasonable agreement with the prediction (line) from Eq. (9), without the use of any fitting parameters.

To predict the delay time τ_d and the slowed probe group velocity v_g , we refer to Eqs. (13) and (14), which use just the power-broadened component of Γ_{EIT} . For intensities $I = 3$ and 1.2 mW/cm^2 as in Fig. 9, the calculated delays τ_d are $72 \mu\text{s}$ (yielding a predicted v_g of 347 m/s) and $181 \mu\text{s}$ (predicted $v_g = 138 \text{ m/s}$), respectively. The predicted v_g -values are a factor two to three slower than the observed v_g -values in Figs. 9(a) and 9(b). To make more accurate predictions, we must move away from an idealized three-level atom model and include the full hyperfine structure (Fig. 3), which is beyond the scope of this article.¹⁹

B. Role of EIT transparency window

Figure 9(a) highlights the importance of the EIT process. The squat data-waveform is the transmitted probe pulse when the pump beam is blocked causing the EIT window to cease to exist: Large absorption and no slowing is observed. The transmitted power of the slow pulse for the unblocked pump is $\sim 20\%$ – 25% of the incident probe power, while for the blocked pump is less than 5% .

To further highlight the important role played by EIT, we show in Fig. 9(c) what happens if we select a pulse duration for which the probe bandwidth does not fit inside the EIT transparency window. The input Gaussian pulse in this case, $\sim 20 \mu\text{s}$ (which yields a $1/e$ -pulse bandwidth of $\sim 10 \text{ kHz}$), is nearly an order of magnitude shorter than the $170 \mu\text{s}$ pulse employed in Figs. 9(a) and 9(b). Thus, in the case of Fig. 9(c) the pulse bandwidth is comparable to the EIT window which ranges from a few kHz to $\leq 30 \text{ kHz}$ for our experiments. The frequency components of this pulse that do not fit within the EIT window are not slowed and are instead significantly absorbed. This leads to significant temporal stretching and distortion of the pulse (we scaled the vertical size of the reference pulse to resemble the transmitted probe).

In fact, some probe pulse broadening is visible even in the case of the slowest group velocity measured in Fig. 9(b). In

this case, higher frequency components of the 170 μs Gaussian probe pulse ($1/e$ -frequency bandwidth ~ 1 kHz) extrude past the 10.8 kHz Lorentzian EIT transparency window, and are strongly absorbed. This causes an effective narrowing of the probe bandwidth, which leads to a broadening of the pulse duration.

C. Slow group velocity versus pump intensity

In Fig. 10, we plot the experimentally observed slow light group velocity for several pump intensities at three different vapor temperatures. The observed temperature dependence of v_g is in accordance with what we expect from Eq. (13): N increases with T (see Sec. S2 D in supplementary material¹¹) causing v_g to decrease.

At a fixed temperature, we surmise from Fig. 10 that two competing slow light effects occur when we vary the pump intensity. The linear increase in v_g with increasing pump intensity I is expected from Eq. (13). Recall that this originates from the power-broadening of the EIT transparency window as described by Eq. (9), thereby reducing the “tightness of the pinch” of the “wrinkle” in the real refractive index n_r at $\Delta_p = 0$ in Figs. 2(d) and 2(f).

However, it is obvious that one cannot keep reducing the pump intensity to achieve lower and lower group velocities as there is no slow light in the absence of a pump.

At really low pump intensities, the weak probe assumption starts to break down and, as mentioned in Sec. III C already, the population of atoms being pumped to the dark state may decline to the point that the probe pulse appears to start speeding up again.

Group velocities of several thousand m/s suffice for most cutting-edge experiments on quantum memory and image storage in warm vapor.^{5,6} At higher temperatures, the density increases, but so do spin depolarization mechanisms such as Rb–Rb spin exchange collisions and radiation trapping, as indicated in Sec. III B. In vapor cells that use paraffin-based anti-spin relaxation coatings instead of buffer gas, temperatures exceeding 80 °C may cause coating breakdown. Coatings, such as OTS (octadecyltrichlorosilane), permit higher temperatures.^{39,40}

VIII. CONCLUSION

We have presented detailed theoretical and experimental undergraduate-friendly instructions on how to produce light pulses propagating through warm alkali vapor with speeds as

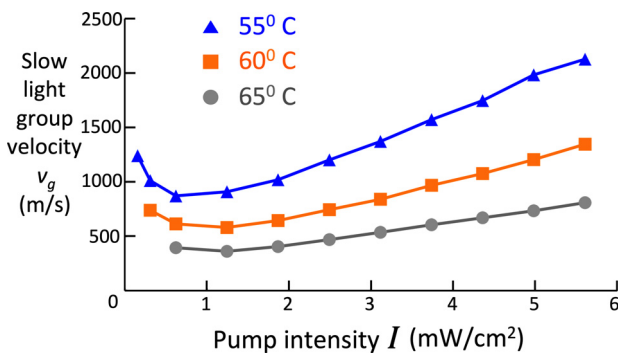


Fig. 10. Slow light at different pump intensities I and temperatures T (lines drawn to guide the eye). All measurements are in isotopically pure ^{87}Rb vapor with 10 Torr Ne.

low as few hundred m/s, emphasizing the role played by EIT in the production of slow light.

The experimental setup described here is remarkably versatile. It can be used for investigations into slow and stored light, including detailed measurements of the pulse delay τ_d as the pulse width τ_p is varied, and further measurement of the subtle Ramsey narrowing seen at the EIT line-center in Fig. 8 as the pump and probe beam sizes are varied.³³ By slightly varying the angle between the pump and probe beams, one can study EIT linewidth-narrowing due to the spatial localization of alkali atoms from frequent velocity-changing collisions with the buffer gas.⁴¹ Furthermore, one may study how atomic diffusion degrades storage times for slow light pulses⁴² of various transverse profiles, e.g., Laguerre–Gaussian⁴³ and Bessel beams,⁴⁴ which possess topological phase features that permit significantly more robust storage in comparison to the usual Gaussian beams. The setup may be adapted for innovative magnetometry with potential applications in magnetic induction tomography and the detection of concealed objects.^{45,46}

ACKNOWLEDGMENTS

The authors gratefully acknowledge the support by the U. S. Army Research Laboratory and the U. S. Army Research Office under Grant No. W911NF2110120. The authors appreciate insightful discussions with Drs. Irina Novikova, David Phillips, Ofer Firstenberg, and Ran Finkelstein, and invaluable detailed feedback from the three anonymous referees and from the editor. The authors thank Hong Cai, Kaleb Campbell, Richard Jackson, Dillon deMedeiros, Bradley Worth, Amanda Day, Somaya Madkhaly, Yuhong (Iris) Zhang, Peter Harnish, and Jason Barkeloo for help during the initial setup. The authors thank the Miami University Instrumentation Laboratory for crucial help in machining and electronics.

AUTHOR DECLARATIONS

The authors have no conflicts to disclose.

Author Contributions

Kenneth DeRose and Kefeng Jiang contributed equally to this work.

^{a)}ORCID: 0000-0003-2354-3617.

^{b)}Electronic mail: balis@miamioh.edu, ORCID: 0000-0002-8677-305X.

¹L. V. Hau, S. E. Harris, Z. Dutton, and C. H. Behroozi, “Light speed reduction to 17 metres per second in an ultracold atomic gas,” *Nature* **397**, 594–598 (1999).

²M. Kash, V. Sautenkov, A. Zibrov, L. Hollberg, G. Welch, M. Lukin, Y. Rostovtsev, E. Fry, and M. Scully, “Ultraslow group velocity and enhanced nonlinear optical effects in a coherently driven hot atomic gas,” *Phys. Rev. Lett.* **82**, 5229–5232 (1999).

³S. Harris, J. Field, and A. Imamoglu, “Nonlinear optical processes using electromagnetically induced transparency,” *Phys. Rev. Lett.* **64**, 1107–1110 (1990).

⁴S. Harris, “Electromagnetically induced transparency,” *Phys. Today* **50**(7), 36–42 (1997).

⁵I. Novikova, R. Walsworth, and Y. Xiao, “Electromagnetically induced transparency-based slow and stored light in warm atoms,” *Laser Photonics Rev.* **6**, 333–353 (2012).

⁶L. Ma, O. Slattery, and X. Tang, “Optical quantum memory based on electromagnetically induced transparency,” *J. Opt.* **19**, 043001 (2017).

- ⁷M. Afzelius, N. Gisin, and H. D. Riedmatten, “Quantum memory for photons,” *Phys. Today* **68**(12), 42–47 (2015).
- ⁸C. Adams, J. Pritchard, and J. Schaffer, “Rydberg atom quantum technologies,” *J. Phys. B* **53**(1), 012002 (2020).
- ⁹N. Belcher, E. Mikhailov, and I. Novikova, “Atomic clocks and coherent population trapping: Experiments for undergraduate labs,” *Am. J. Phys.* **77**, 988–998 (2009).
- ¹⁰See, for example, A. Zheng, A. Green, M. Crescimanno, and S. O’Leary, “Electromagnetically-induced-transparency intensity-correlation power broadening in a buffer gas,” *Phys. Rev. A* **93**, 043825 (2016).
- ¹¹See supplementary material at <https://www.scitation.org/doi/suppl/10.1119/5.0128967> for background details on the basic physics behind EIT, in addition to useful technical details on magnetic shielding and heating of the alkali vapor cell, and the construction of a solenoid to apply a small magnetic field to the vapor cell.
- ¹²A. J. Olson and S. K. Mayer, “Electromagnetically induced transparency in rubidium,” *Am. J. Phys.* **77**(2), 116–121 (2009).
- ¹³T. Pang, “Electromagnetically induced transparency,” *Am. J. Phys.* **69**(5), 604–606 (2001).
- ¹⁴K. McDonald, “Slow light,” *Am. J. Phys.* **68**(3), 293–294 (2000).
- ¹⁵M. Fleischhauer and G. Juzeliūnas, “Slow, stored, and stationary light,” in *Optics in Our Time*, edited by M. Al-Amri, M. El-Gomati, and M. Zubairy (Springer, New York, 2016), pp. 359–385.
- ¹⁶P. W. Milonni and J. H. Eberly, *Laser Physics* (Wiley, New York, 2010).
- ¹⁷B. E. A. Saleh and M. Teich, *Fundamentals of Photonics*, 3rd ed. (Wiley, New York, 2019); provides the Kramer–Kronig relations for the real and imaginary parts of the electric susceptibility χ' and χ'' , respectively, where $\chi' = 2(n_r - 1)$ and $\chi'' = c\alpha/\omega_p$.
- ¹⁸Our definition of Ω_c, Ω_p follows. Refs. 5, 16, and 19. Some authors omit the 2 in the denominator (e.g., Refs. 25 and 27).
- ¹⁹M. Lukin, M. Fleischhauer, A. Zibrov, H. Robinson, V. Velichansky, L. Hollberg, and M. Scully, “Spectroscopy in dense coherent media: Line narrowing and interference effects,” *Phys. Rev. Lett.* **79**, 2959–2962 (1997).
- ²⁰M. Fleischhauer and M. Lukin, “Quantum memory for photons: Dark-state polaritons,” *Phys. Rev. A* **65**(2), 022314 (2002).
- ²¹Equation (14) is identical to Eq. (6) in Ref. 5, Eq. (38) in Ref. 20.
- ²²M. Klein, M. Hohensee, Y. Xiao, R. Kalra, D. Phillips, and R. Walsworth, “Slow-light dynamics from electromagnetically induced transparency spectra,” *Phys. Rev. A* **79**(5), 053833 (2009).
- ²³Equation (15) is identical to Eq. (39) in Ref. 20.
- ²⁴N. B. Phillips, A. V. Gorshkov, and I. Novikova, “Optimal light storage in atomic vapor,” *Phys. Rev. A* **78**(2), 023801 (2008).
- ²⁵D. Steck, see <https://steck.us/alkalidata/> for reference data on the D spectral lines for Rb.
- ²⁶See Fig. 7.5 on p. 141 of Ref. 27.
- ²⁷M. Auzinsh, D. Budker, and S. M. Rochester, *Optically Polarized Atoms* (Oxford U.P., New York, 2010).
- ²⁸W. Happer, “Optical pumping,” *Rev. Mod. Phys.* **44**(2), 169–249 (1972).
- ²⁹J. E. Thomas and W. W. Quivers, Jr., “Transit-time effects in optically pumped coupled three-level systems,” *Phys. Rev. A* **22**(5), 2115–2121 (1980).
- ³⁰E. Arimondo, “Relaxation processes in coherent population trapping,” *Phys. Rev. A* **54**(3), 2216–2223 (1996).
- ³¹A. Matsko, I. Novikova, M. Scully, and G. Welch, “Radiation trapping in coherent media,” *Phys. Rev. Lett.* **87**(13), 133601 (2001).
- ³²See Ref. 16, Sec. 4.11 or Ref. 27, Sec. 9.1.
- ³³Y. Xiao, I. Novikova, D. F. Phillips, and R. Walsworth, “Diffusion-induced Ramsey narrowing,” *Phys. Rev. Lett.* **96**, 043601 (2006).
- ³⁴M. Shuker, O. Firstenberg, Y. Sagi, A. Ben-kish, N. Davidson, and A. Ron, “Ramsey-like measurement of the decoherence rate between Zeeman sublevels,” *Phys. Rev. A* **78**, 063818 (2008).
- ³⁵M. D. Rotondaro and G. P. Perram, “Collisional broadening and shift of the rubidium D1 and D2 lines ($5^2S_{1/2} \rightarrow 5^2P_{1/2}, 5^2P_{3/2}$) by rare gases, H₂, D₂, N₂, CH₄ and CF₄,” *J. Quant. Spectrosc. Radiat. Transfer* **57**, 497–507 (1997).
- ³⁶See, for example. Ref. 16, Sec. 3.9, pp 105–108.
- ³⁷J. Kleykamp, A. Hachtel, D. Kane, M. Marshall, N. Souther, P. Harnish, and S. Bali, “Measurement of sub-natural line width AC Stark shifts in cold atoms: An experiment for an advanced undergraduate laboratory,” *Am. J. Phys.* **79**(12), 1211–1217 (2011); see Fig. 5 and accompanying text in.
- ³⁸A. Hachtel, J. Kleykamp, D. Kane, M. Marshall, B. Worth, J. Barkeloo, J. Kangara, J. Camenisch, M. Gillette, and S. Bali, “An undergraduate measurement of radiative broadening in atomic vapor,” *Am. J. Phys.* **80**(8), 740–743 (2012); **81**(6), 471 (2013).
- ³⁹See, private communication; see also “Technical Info” on the Precision Glassblowing, Inc. website.
- ⁴⁰H. Chi, W. Quan, J. Zhang, L. Zhao, and J. Fang, “Advances in anti-relaxation coatings of alkali-metal vapor cells,” *Appl. Surf. Sci.* **501**, 143897 (2020).
- ⁴¹M. Shuker, O. Firstenberg, R. Pugatch, A. Ben-Kish, A. Ron, and N. Davidson, “Angular dependence of Dicke-narrowed electromagnetically induced transparency resonances,” *Phys. Rev. A* **76**(2), 023813 (2007).
- ⁴²M. Shuker, O. Firstenberg, R. Pugatch, A. Ron, and N. Davidson, “Storing images in warm atomic vapor,” *Phys. Rev. Lett.* **100**, 223601 (2008).
- ⁴³R. Pugatch, M. Shuker, O. Firstenberg, A. Ron, and N. Davidson, “Topological stability of stored optical vortices,” *Phys. Rev. Lett.* **98**, 203601 (2007).
- ⁴⁴S. Smartsev, R. Chriki, D. Eger, O. Firstenberg, and N. Davidson, “Structured beams invariant to coherent diffusion,” *Opt. Express* **28**(22), 33708–33717 (2020).
- ⁴⁵A. Wickenbrock, F. Tricot, and F. Renzoni, “Magnetic induction measurements using an all-optical ⁸⁷Rb atomic magnetometer,” *Appl. Phys. Lett.* **103**, 243503 (2013).
- ⁴⁶C. Deans, L. Marmugi, and F. Renzoni, “Through-barrier electromagnetic imaging with an atomic magnetometer,” *Opt. Express* **25**(15), 17911–17917 (2017).

SUPPLEMENTARY NOTES

Producing slow light in warm alkali vapor using electromagnetically induced transparency

Kenneth DeRose[†], Kefeng Jiang[†], Jianqiao Li, Macbeth Julius, Linzhao Zhuo, Scott Wenner, and Samir Bali^{*}

Department of Physics, Miami University, Oxford, Ohio 45056-1866, USA

Compiled November 27, 2022

In order to complement the undergraduate-friendly detailed experimental description in the main article, here, in Sec. S1, we provide background details for the basic physics behind electromagnetically induced transparency (EIT). We endeavor to keep the discussion amenable to advanced juniors and seniors. Furthermore, in Sec. S2 we provide useful technical details on magnetic shielding of the alkali vapor cell in order to suppress stray magnetic fields in the laser-atom interaction region below 0.2 mG, the implementation of a heater assembly in order to increase the atomic density participating in EIT, and the construction of a solenoid to apply a small magnetic field to the vapor cell in order to enable Zeeman EIT. A price and vendor list for parts is provided in Table 1. © 2022 Optical Society of America

S1. Theoretical Background

The theoretical discussion of EIT and slow light centers around calculating the complex refractive index $n = n_r + in_i$ of the medium. The imaginary part n_i yields the absorption spectrum, where EIT in atomic media is revealed as a narrow transparency window near resonance. The real part n_r yields the group velocity of light propagating through the medium. Slow light is revealed as a consequence of the steep frequency-variation of n_r within the EIT transparency window.

We begin by writing down the Hamiltonian and the Schrödinger equation for the illuminated three-level atomic model in Fig. 1 (reproduced in Fig. S1 a), and derive the widely used optical Bloch equations. Next, we use these equations to calculate the complex refractive index n of a dilute gas (or vapor), and reveal the required conditions for EIT and slow light. We follow closely the treatment in Ref. [1] - however, we define the laser detunings Δ_p and Δ_c opposite in sign to Ref. [1].

A. Hamiltonian for light-atom interaction

If we denote the wavefunction for the atom interacting with an incident light field as $\Psi(\vec{r}, t)$, the time evolution of Ψ is described by the Schrödinger equation

$$i\hbar \frac{\partial \Psi(\vec{r}, t)}{\partial t} = \hat{H} \Psi(\vec{r}, t) = (\hat{H}_0 + \hat{V}) \Psi(\vec{r}, t). \quad (\text{S1})$$

Here, \hat{H} is the Hamiltonian for the system, i.e., the energy operator of the system, acting upon the wavefunction Ψ . Since we are focusing on just the atom and its interaction with the incident field, we may ignore the contribution to the Hamiltonian from the incident field alone (also known as the free field). In that case it is convenient to express the Hamiltonian operator \hat{H} as a sum of two terms: \hat{H}_0 , the bare Hamiltonian which describes the atom in the absence of any external field, and \hat{V} the interaction Hamiltonian which describes the interaction between the atom and the external field.

Typically the outermost electrons of the atom are the least tightly bound and respond most readily to the incident field. Indeed, this is an important reason why alkali atoms are favorites with physicists - relatively low optical energies are needed to resonantly excite the lone valence electron. Further, the interaction of the single electron with the incident field is simple to model. The incident electromagnetic field's electric and magnetic vectors, $\vec{E}(\vec{r}, t)$ and $\vec{B}(\vec{r}, t)$ respectively, interact with the valence electron (negative charge e) through the Lorentz force. The electron speed is non-relativistic, so the effect of the \vec{B} -field may be ignored [2]. The incident \vec{E} -field induces an electric dipole in the atom.

Thus, \hat{V} is given by the potential energy stored in this induced dipole, $\hat{V} = -\vec{d} \cdot \vec{E}(\vec{r}, t)$ where \vec{d} is the induced dipole moment (see Fig. S1(b)) and \vec{r} is the location of

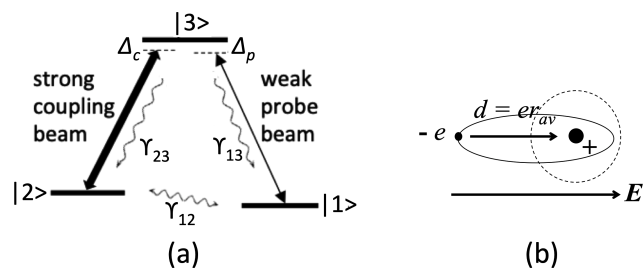


Fig. S1. a) Three-level atomic model from Fig. 1. b) Depiction of an atom showing a lone valence electron orbiting the nucleus (big dot). In the absence of an external field, the mean dipole moment, averaged over an electron revolution, is zero. When illuminated by an electric field \vec{E} , the electron cloud shifts in the opposite direction (elliptical orbit) creating an induced dipole moment \vec{d} of magnitude er_{av} , where $r_{av} (\propto E)$ represents the average displacement between the positive and negative regions of the atom. The polarizability α_p is defined by $\vec{d} = \alpha_p \vec{E}$.

the atomic center of mass. We ignore the variation of \vec{E} over the spatial extent of the atom (\sim nm) because the optical wavelength (\sim hundreds of nm) is much larger.

For the simple three-level atom shown in Fig. S1(a) we denote its states as $|i\rangle$ ($i = 1, 2, 3$), with bare energies ξ_i . Clearly, the states $|i\rangle$ are eigenstates of the bare Hamiltonian \hat{H}_0 , i.e., $\hat{H}_0|i\rangle = \xi_i|i\rangle$ and may be defined to form an orthonormal basis: $\langle i|j\rangle$ is 1 if $i = j$ and 0 otherwise. This means that any arbitrary wavefunction for the three-level atom, such as $\Psi(\vec{r}, t)$ in Eq. (S1), may be expressed as a linear superposition of the states $|i\rangle$ with time-dependent weighting coefficients a_i :

$$\Psi(\vec{r}, t) = \sum_{i=1}^3 a_i(t)|i\rangle, \text{ where } \sum_{i=1}^3 |a_i|^2 = 1. \quad (\text{S2})$$

Substituting this into Eq. (S1), and introducing $\hbar\omega_{ij} \equiv \xi_i - \xi_j$ for $i \neq j$, we project the resultant equation onto each of the $\langle i|$ -states to obtain

$$\begin{aligned} i\hbar\dot{a}_1 &= V_{13}a_3 \\ i\hbar\dot{a}_2 &= \hbar\omega_{21}a_2 + V_{23}a_3 \\ i\hbar\dot{a}_3 &= \hbar\omega_{31}a_3 + V_{32}a_2 + V_{31}a_1, \end{aligned} \quad (\text{S3})$$

where ξ_1 is set equal to 0. We assume that the $1 \leftrightarrow 2$ transition is dipole-forbidden, i.e., $|1\rangle$ and $|2\rangle$ are not coupled by a dipole transition. In Eq. (S3) the interaction terms V_{ij} are: $V_{ij} = \langle i| -\hat{d}|j\rangle \cdot \vec{E}(t) = -\vec{d}_{ij} \cdot \vec{E}$. Note that the \vec{d}_{ii} terms are zero because the spatial states $|i\rangle$ have well-defined parity and \hat{d} is an odd spatial function. Also note that $\vec{d}_{ij}^* = \vec{d}_{ji}$ (see Eq. (9.3.8) in Ref. [1]).

Assuming the incident field $\vec{E}(t)$ to be a sum of the coupling and probe fields each of which is a monochromatic plane-wave of frequency ω_c and ω_p , amplitude E_c and E_p , and polarization unit vectors \vec{e}_c and \vec{e}_p , we write:

$$\hat{E}(t) = \frac{1}{2}\vec{e}_c E_c e^{-i\omega_c t} + \frac{1}{2}\vec{e}_p E_p e^{-i\omega_p t} + c.c., \quad (\text{S4})$$

where *c.c.* denotes complex conjugate, and we have assumed the atom to be located at the origin for convenience [3]. Substituting Eq. (S4) in Eq. (S3) we find the optical Bloch equations:

$$\begin{aligned} \dot{a}_1 &= \frac{i}{2\hbar}\vec{d}_{13} \cdot (\vec{e}_p E_p e^{-i\omega_p t} + \vec{e}_p^* E_p^* e^{i\omega_p t}) a_3 \\ \dot{a}_2 &= -i\omega_{21}a_2 + \frac{i}{2\hbar}\vec{d}_{23} \cdot (\vec{e}_c E_c e^{-i\omega_c t} + \vec{e}_c^* E_c^* e^{i\omega_c t}) a_3 \\ \dot{a}_3 &= -i\omega_{31}a_3 + \frac{i}{2\hbar}\vec{d}_{32} \cdot (\vec{e}_c E_c e^{-i\omega_c t} + \vec{e}_c^* E_c^* e^{i\omega_c t}) a_2 \\ &\quad + \frac{i}{2\hbar}\vec{d}_{31} \cdot (\vec{e}_p E_p e^{-i\omega_p t} + \vec{e}_p^* E_p^* e^{i\omega_p t}) a_1. \end{aligned} \quad (\text{S5})$$

In order to solve the differential equations in Eq. (S5), we take a cue from the case of zero incident fields (i.e., $E_p = E_c = 0$), for which the solutions are trivially obtained as $a_1(t) = a_1(0)$, $a_2(t) = a_2(0)e^{-i\omega_{21}t}$, and $a_3(t) = a_3(0)e^{-i\omega_{31}t}$. Next, we guess at the nonzero incident field solutions by simply replacing the constants

$a_i(0)$ in the zero-incident field solutions with the slowly-varying coefficients $c_i(t)$ (which are as yet unknown, and must be solved for as shown below), and replacing ω_{31} and ω_{32} by ω_p and ω_c respectively (because we expect the driving frequencies ω_c, ω_p to dominate after long times). This yields

$$\begin{aligned} a_1(t) &= c_1(t) \\ a_2(t) &= c_2(t)e^{-i(\omega_p - \omega_c)t} \\ a_3(t) &= c_3(t)e^{-i\omega_p t}. \end{aligned} \quad (\text{S6})$$

We now replace the a_i 's in Eq. (S5) with the c_i 's from Eq. (S6), and invoke the rotating wave approximation (RWA) which lets us ignore terms oscillating at twice the optical frequency because they average to zero (measurement times exceed a few optical cycles). We obtain:

$$\begin{aligned} \dot{c}_1 &= i\Omega_p^* c_3 \\ \dot{c}_2 &= i(\Delta_p - \Delta_c)c_2 + i\Omega_c^* c_3 \\ \dot{c}_3 &= i\Delta_p c_3 + i\Omega_c c_2 + i\Omega_p c_1. \end{aligned} \quad (\text{S7})$$

where we have defined the probe and coupling Rabi frequencies as $\Omega_p \equiv \vec{d}_{31} \cdot \vec{e}_p E_p / 2\hbar$ and $\Omega_c \equiv \vec{d}_{32} \cdot \vec{e}_c E_c / 2\hbar$, respectively. The Rabi frequency is the rate at which the state-occupation probability of a resonantly excited two-level atom oscillates between the excited and ground states. In writing Eq. (S7) we have introduced the pump and probe detunings $\Delta_c \equiv \omega_c - \omega_{32}$ and $\Delta_p \equiv \omega_p - \omega_{31}$. Further, note that in going from Eq. (S5) to Eq. (S7) we have used $\vec{d}_{13} \cdot \vec{e}_p^* E_p^* / 2\hbar = \vec{d}_{31}^* \cdot \vec{e}_p^* E_p^* / 2\hbar = \Omega_p^*$, and a similar argument to derive Ω_c^* .

B. Dark and bright states in EIT

An important question is: What are the new eigenstates for the Hamiltonian in Eq. (S1) describing the three-level atomic system in Fig. S1(a) under illumination by the coupling and probe fields? To answer this question, we re-cast Eq. (S7) in a form that enables us to write down the Hamiltonian under the rotating wave approximation which we denote by \hat{H}_{RWA} . Eq. (S7) now yields:

$$i\hbar \begin{pmatrix} \dot{c}_1 \\ \dot{c}_2 \\ \dot{c}_3 \end{pmatrix} = -\hbar \begin{pmatrix} 0 & 0 & \Omega_p^* \\ 0 & \Delta_p - \Delta_c & \Omega_c^* \\ \Omega_p & \Omega_c & \Delta_p \end{pmatrix} \begin{pmatrix} c_1 \\ c_2 \\ c_3 \end{pmatrix}, \quad (\text{S8})$$

We rewrite the Schrodinger equation in Eq. (S1) as $i\hbar|\dot{\Psi}_{RWA}\rangle = \hat{H}_{RWA}|\Psi_{RWA}\rangle$ where $|\Psi_{RWA}\rangle = \sum_{i=1}^3 c_i(t)|i\rangle$, and compare with Eq. (S8) to find:

$$\hat{H}_{RWA} = -\hbar \begin{pmatrix} 0 & 0 & \Omega_p^* \\ 0 & \Delta_p - \Delta_c & \Omega_c^* \\ \Omega_p & \Omega_c & \Delta_p \end{pmatrix}. \quad (\text{S9})$$

Setting the pump and probe detunings equal to zero for simplicity, we deduce three eigenenergies:

$$(\lambda_0, \lambda_{\pm}) = (0, \mp\hbar\Omega) \text{ for } \Delta_p = \Delta_c = 0, \quad (\text{S10})$$

where Ω is a generalized Rabi frequency defined as $\Omega \equiv \sqrt{|\Omega_c|^2 + |\Omega_p|^2}$. The three orthonormal eigenstates corresponding to these eigenvalues are:

$$\begin{aligned} |0\rangle &= \frac{1}{\Omega} (\Omega_c |1\rangle - \Omega_p |2\rangle) \\ |\pm\rangle &= \frac{1}{\sqrt{2}} \left(\frac{\Omega_p^* |1\rangle + \Omega_c^* |2\rangle}{\Omega} \mp |3\rangle \right). \end{aligned} \quad (\text{S11})$$

Eq. (S11) reveals a few key insights. An atom that happens to be in eigenstate $|0\rangle$ has no overlap with state $|3\rangle$, hence cannot excite into state $|3\rangle$. For this reason we refer to $|0\rangle$ as a *dark state*. In EIT experiments, the probe is much weaker than the coupling field ($\Omega_p \ll \Omega_c$), yielding the result $|0\rangle \approx |1\rangle$. Further, if we re-cast the two non-dark states $|\pm\rangle$ in Eq. (S11) in terms of two new *non-stationary* states $|+\rangle$ and $|-\rangle$: $|\pm\rangle = \frac{1}{\sqrt{2}} (|-\rangle \pm |+\rangle)$ we see that, in this weak probe approximation, $|+\rangle \approx |2\rangle$ and $|-\rangle \approx |3\rangle$. Here, $|+\rangle$ and $|-\rangle$ are not stationary states because the strong coupling field oscillates the atoms back and forth between $|2\rangle$ and $|3\rangle$. We therefore refer to the $|+\rangle \approx |2\rangle$ -state, which is strongly coupled to $|3\rangle$, as the *bright state*. Thus, in the case of on-resonant pump and probe excitations and a weak probe, the states $|1\rangle$ and $|2\rangle$ in the three-level system of Fig. S1(a) form a dark state and bright state, respectively.

The formation of a dark state - this new eigenstate into which resonantly illuminated three-level atoms are pumped - lies at the heart of EIT: These atoms are transparent to the resonant illumination.

C. Density-matrix: Populations, coherences, and decay

The previous section shows the formation of a dark state which leads to a “transparency window” called EIT. But what is the spectral width of this transparency window? Can we estimate the amplitude of the window, i.e., the EIT contrast? To address these questions we need to include decay processes into our discussion. The density matrix formalism allows for simple phenomenological inclusion of these processes.

For an illuminated three-level atom, we introduce the probability density matrix $\hat{\rho}$ which is a 3×3 matrix with diagonal elements $\rho_{ii} \equiv c_i c_i^*$ representing the *probability* of the atom being in state $|i\rangle$ (i.e, the population in state $|i\rangle$ for a sample of many atoms) and off-diagonal elements $\rho_{ij} \equiv c_i c_j^*$ ($i \neq j$) representing the *coherence* (or strength or amplitude) of the induced dipole operator \hat{V} between states $|i\rangle$ and $|j\rangle$, or, in other words, the complex amplitude of the electron displacement \vec{r}_{av} in Fig. S1(b). The density matrix, rather than the dark state, has a tangible connection to the lab because experiments measure probabilities and coherences, not eigenstates.

As discussed in the previous section, a strong pump and weak probe causes level $|1\rangle$ in Fig. S1(a) to take on the role of the dark state, meaning that an atom, once it falls into $|1\rangle$, stays there, unable to interact with the light any more. On the other hand, an atom in level $|2\rangle$, the bright state, once optically excited to

$|3\rangle$, can either fall into $|1\rangle$ where it then stays, or fall into $|2\rangle$ where it is re-excited to $|3\rangle$ and the process repeats. Over many absorption-emission cycles, this causes the atomic population to be progressively transferred, or “optically pumped”, into level $|1\rangle$, meaning that $\rho_{11} \approx 1$ and $\rho_{22} \approx \rho_{33} \approx 0$ (also, $\rho_{32} \approx 0$). In this weak probe approximation we find from Eq. (S7):

$$\begin{aligned} \dot{\rho}_{13} &= c_1 \dot{c}_3^* + \dot{c}_1 c_3^* = -i\Delta_p \rho_{13} - i\Omega_c^* \rho_{12} - i\Omega_p^* \\ \dot{\rho}_{12} &= c_1 \dot{c}_2^* + \dot{c}_1 c_2^* = -i(\Delta_p - \Delta_c) \rho_{12} - i\Omega_c \rho_{13} \\ \dot{\rho}_{23} &\approx 0. \end{aligned} \quad (\text{S12})$$

We have so far ignored decay and relaxation/line-broadening mechanisms. Elastic collisions, for example, cause an exponential decay of the phase of the induced dipole moments ρ_{12} and ρ_{13} , while inelastic collisions cause an exponential decay of their magnitudes. For warm samples ($T = 55^\circ\text{C} - 65^\circ\text{C}$ in our experiments), Doppler broadening is another significant line-broadening mechanism. We denote all decay processes from $3 \rightarrow 1$ by the optical decoherence rate γ_{13} . The dominant contributions to γ_{13} in our experiment come from Doppler broadening and Rb collisions with the Neon buffer gas (see Sec. 3C). We lump all elastic and inelastic damping processes causing relaxation of the induced dipole moment for the *non-allowed* transition 1 to 2 into γ_{12} , the ground state decoherence rate. Recall that $\gamma_{12} \ll \gamma_{13}$ in our experiments.

Including these exponential dephasing terms in Eq. (S12) we obtain

$$\begin{aligned} \dot{\rho}_{13} &= -i(\Delta_p - i\gamma_{13}) \rho_{13} - i\Omega_c^* \rho_{12} - i\Omega_p^* \\ \dot{\rho}_{12} &= -i(\Delta_p - \Delta_c - i\gamma_{12}) \rho_{12} - i\Omega_c \rho_{13}. \end{aligned} \quad (\text{S13})$$

We are interested in solutions to Eq. (S13) for times $t \gg 1/\gamma_{12}, 1/\gamma_{13}$. In this long-time limit, the atomic variables have “relaxed” to their steady-state values and are no longer functions of time. Setting $\dot{\rho}_{12}$ and $\dot{\rho}_{13}$ equal to zero, we obtain the “steady-state solutions”:

$$\rho_{13} = \frac{\Omega_p^* (\Delta_p - \Delta_c - i\gamma_{12})}{|\Omega_c|^2 - (\Delta_p - \Delta_c - i\gamma_{12})(\Delta_p - i\gamma_{13})}. \quad (\text{S14})$$

Eq. (S13) and Eq. (S14) are derived in Ref. [1], except that our equations include nonzero pump detuning Δ_c .

D. Probe-induced dipole moment, polarizability, refractive index, and absorption

We may evaluate the expectation value of the induced dipole moment operator $\hat{\vec{d}}$ in the state Ψ , in terms of the density matrix coherences above. From Eq. (S2) we obtain $\langle \hat{\vec{d}} \rangle = \sum_{i \neq j}^3 a_i^* a_j \vec{d}_{ij}$ (recall from Sec. S1A that the \vec{d}_{ii} terms are zero). Using Eq. (S6) we find for the dipole moment induced by the coupling and probe fields:

$$\langle \hat{\vec{d}} \rangle = \rho_{12} e^{i(\omega_p - \omega_c)t} \vec{d}_{21} + \rho_{13} e^{i\omega_p t} \vec{d}_{31} + c.c. \quad (\text{S15})$$

If our goal is to calculate the polarizability, refractive index, and absorption as detected by the *probe* beam propagating through the coherently pumped three-level atomic sample, we should focus in Eq. (S15) on the probe-induced term in which ρ_{13} appears as the weighting coefficient of the induced dipole moment \vec{d}_{31} oscillating at the probe frequency. Extracting this term from Eq. (S15) we write for the *probe-induced dipole moment*, denoted by $\langle \hat{\vec{d}} \rangle_{probe}$:

$$\langle \hat{\vec{d}} \rangle_{probe} = \rho_{13} e^{i\omega_p t} \vec{d}_{31} + c.c. \quad (\text{S16})$$

The induced dipole moment is also defined in terms of the polarizability, as in the caption to Fig. S1(b). From Eq. (S4), we write for the *probe-induced polarizability* α_p :

$$\langle \hat{\vec{d}} \rangle_{probe} = \alpha_p \left(\frac{1}{2} \vec{\epsilon}_p E_p e^{-i\omega_p t} + c.c. \right). \quad (\text{S17})$$

Equating terms oscillating at the same frequency in Eq. (S16) and Eq. (S17), and taking the dot product with $\vec{\epsilon}_p^*$ on both sides (note: $\vec{\epsilon}_p \cdot \vec{\epsilon}_p^* = 1$), we find the polarizability α_p in terms of the density matrix element ρ_{13} :

$$\frac{1}{2} \alpha_p E_p = \rho_{31} \vec{d}_{13} \cdot \vec{\epsilon}_p^*. \quad (\text{S18})$$

We substitute the complex conjugate of Eq. (S14) in Eq. (S18) to obtain for the probe-induced polarizability

$$\alpha_p = \frac{|\mu_{13}|^2}{\hbar} \frac{\Delta_p - \Delta_c + i\gamma_{12}}{|\Omega_c|^2 - (\Delta_p - \Delta_c + i\gamma_{12})(\Delta_p + i\gamma_{13})}, \quad (\text{S19})$$

where we used the definition of Ω_p as stated immediately after Eq. (S7), and we introduced the symbol $\mu_{13} = \vec{d}_{13} \cdot \vec{\epsilon}_p^*$ to denote the projection of the transition dipole moment on the direction of the field polarization.

The relation between the macroscopic refractive index and the polarizability is well-known from undergraduate electrodynamics [4]. For a linear non-magnetic medium with no free currents and dielectric constant ϵ we obtain for the *refractive index n detected by the probe*:

$$n = \sqrt{\epsilon} = \sqrt{1 + N\alpha_p/\epsilon_0} \underset{n \sim 1}{\overset{\text{gas}}{\approx}} 1 + N\alpha_p/2\epsilon_0, \quad (\text{S20})$$

where N is the atomic density, or more precisely, the number of atomic dipoles per unit volume, ϵ_0 is the dielectric permittivity of vacuum, and we have used the fact that $n \sim 1$ for a gas or vapor. Clearly, from Eq. (S19) and Eq. (S20), n is complex, i.e., we may write $n = n_r + i n_i$.

The *probe absorption*, denoted by α , and the imaginary refractive index n_i are straightforwardly related. Consider the simplest case of a plane wave $\vec{E}(z, t) = \vec{E}_0 e^{i(kz - \omega t)}$ propagating in the z -direction through a medium, with the well-known wave relation $k = n\omega/c$. This wave attenuates according to Beer's Law which states: $I(z) = I_0 \exp(-\alpha z)$, where I_0 is the intensity at $z = 0$, and α is the attenuation coefficient. The incident

intensity attenuates exponentially due to both scattering and absorption - the latter dominates at near-resonance incident frequencies, in which case we may simply refer to α as the absorption coefficient. The exponent αz is known as the *optical depth*. The on-resonance optical depth seen by the probe as it traverses an atomic sample of length L (with the strong coupling beam turned off) is denoted by OD in the main article [5–7].

Substituting the complex expression for n into the plane wave amplitude above, we find $\vec{E}(z, t) = \vec{E}_0 e^{-n_i \omega z/c} e^{i(n_r \omega z/c - \omega t)}$, from which we derive $I(z) = I_0 \exp(-2n_i \omega z/c)$. Comparing this relation with Beer's Law we arrive at the well-known relation between the absorption coefficient and the imaginary refractive index:

$$\alpha = 2n_i \omega/c. \quad (\text{S21})$$

Substituting Eq. (S19) in Eq. (S20), and rationalizing the denominator, we may equate the real and imaginary parts separately in Eq. (S20). Using Eq. (S21), we obtain for the absorption coefficient α :

$$\alpha = \frac{N\omega_p}{\epsilon_0 c} \frac{|\mu_{13}|^2}{\hbar} \times \frac{\gamma_{13} \Delta'^2 + \gamma_{12}(\gamma_{12} \gamma_{13} + |\Omega_c|^2)}{[\Delta_p \Delta' - \gamma_{12} \gamma_{13} - |\Omega_c|^2]^2 + [\gamma_{12} \Delta_p + \gamma_{13} \Delta']^2}, \quad (\text{S22})$$

and for the real part of the refractive index n_r

$$n_r = 1 - \frac{N}{2\epsilon_0} \frac{|\mu_{13}|^2}{\hbar} \times \frac{\Delta'(\Delta' \Delta_p - |\Omega_c|^2) + \gamma_{12}^2 \Delta_p}{[\Delta_p \Delta' - \gamma_{12} \gamma_{13} - |\Omega_c|^2]^2 + [\gamma_{12} \Delta_p + \gamma_{13} \Delta']^2}, \quad (\text{S23})$$

where $\Delta' \equiv$ relative pump-probe detuning $\Delta_p - \Delta_c$ (also referred to as the Raman, or two-photon, detuning). Eq. (3) and Eq. (4) in the main article assume $\Delta_c = 0$ to obtain simplified versions of Eq. (S22) and Eq. (S23).

S2. Magnetic shielding, heating the sample, B_z

This section describes the magnetic shielding used to suppress stray magnetic fields thereby creating a “zero gauss chamber”, in which the laser-atom interaction occurs. We describe the solenoid used to apply a small B -field to the alkali sample in a direction co-linear with the laser beam, in order to enable Zeeman EIT. We present our method to degauss the magnetic shields and measure the residual stray magnetic fields after degaussing. Finally, we describe the implementation of a heater system to raise the alkali vapor temperature, in order to increase the atomic density participating in EIT.

A. Zero gauss chamber:

The zero gauss chamber and all the components inside it are shown in Fig. S2. The chamber itself is formed by three layers of mu-metal sheets, each of thickness 0.64 mm, in the form of open concentric cylinders, with close-fitting end caps on the outermost cylinder. Mu-metal

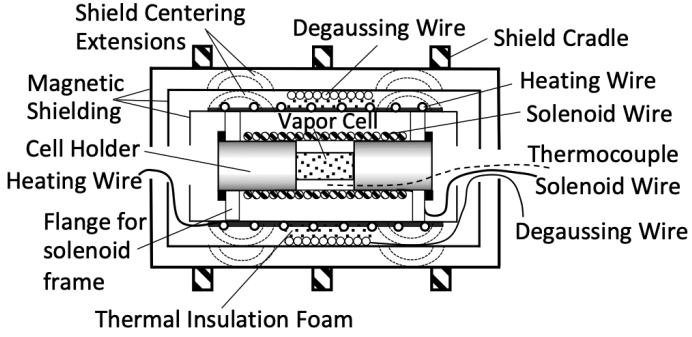


Fig. S2. Cross-section of the zero-gauss chamber.

alloy has high magnetic permeability and is specially engineered to divert incident magnetic field lines to ride along the material walls rather than penetrate through. A hole is cut in the end caps to allow optical access, as well as allow access for wires used for various functions described in the following sub-sections. We purchased commercial shielding (see Table 1), but magnetic shields can be built in-house to cut costs [8]. The manufacturer specifies an attenuation by at least a factor of 1575 of external magnetic fields through our three mu-metal sheets. For example, if the Earth's magnetic field is 0.5 G, the residual magnetic field inside the enclosed cylindrical volume should be 0.3 mG or less. In our case, we find that the residual magnetic field is typically suppressed below 0.2 mG, as described below.

B. Solenoid for creation of B_z :

For slow light investigations based on Zeeman EIT, we rely upon a well-defined quantization axis (the z -axis), which in our case is collinear with the weak external constant magnetic field B_z and the propagation direction of the pump and probe laser beams. B_z creates Zeeman sub-levels, for each of which the magnetic dipole moment precesses around B_z with an angular momentum component $m\hbar$ along the z -axis. For this choice of quantization axis, if the electric field vector of the incident light field is perpendicular to the z -axis, as is the case for our pump and probe beams, the induced (i.e., absorptive and stimulated) transitions among the Zeeman sub-levels obey the selection rule $\Delta m = \pm 1$ [9]. In other words, the absorption depends upon the projections of the precessing magnetic dipoles along the z -axis. Spontaneous emission from the excited Zeeman states is not associated with any special quantization axis and is constrained only by the selection rule $\Delta m = 0, \pm 1$.

The Zeeman magnetic sub-levels are separated via an axial magnetic field $B_z \sim 50$ mG which is created by the solenoid wiring depicted in Fig. S2. Any magnetic field inhomogeneity would cause spatial variation of the dark state, leading to absorption. The uniformity of B_z depends on the length-to-radius ratio of the solenoid. We referred to magnetic field calculations for finite solenoids of different length-to-radius ratios [10], and concluded that a solenoid radius r of 38.1 mm and length L_s of

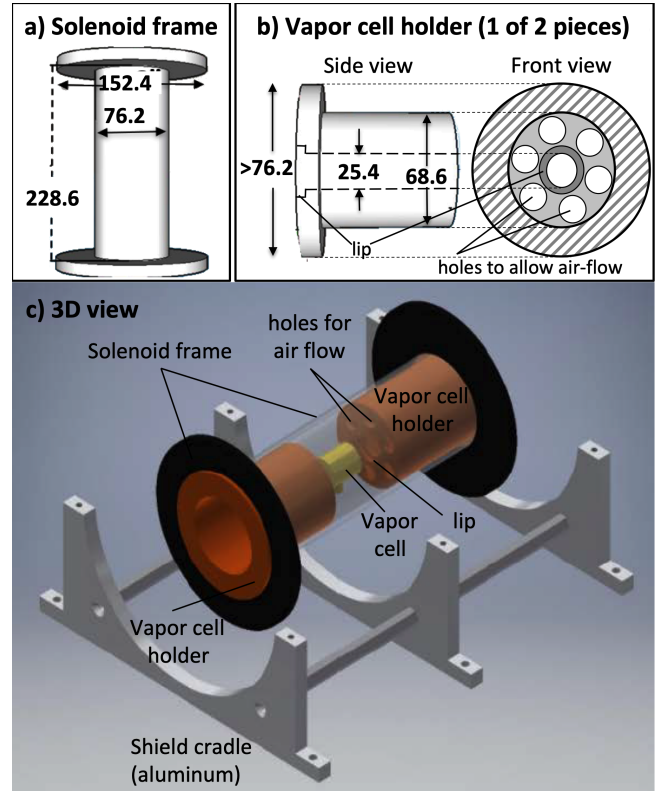


Fig. S3. a) The dimensions (in mm) for the plastic solenoid frame on which the wire is later wrapped. b) Side view of the plastic holder that goes on each end of the vapor cell, and a Front view (i.e., axial view of the holder as seen looking outward from the vapor cell) depicting six through-holes drilled through the entire length of each holder, to allow air-flow. c) A 3D view of the components inside the zero gauss chamber, with the shields and solenoid wiring removed to display the vapor cell and holders. The holders are drawn slightly back to reveal the lip in which the ends of the vapor cell securely fit. The solenoid frame's end-flanges (shown in black) are a close slide-fit inside the innermost mu-metal cylinder.

228.6 mm (ratio of 6:1) yields a uniform magnetic field with a tolerance of 1% within a cylindrical volume 25.4 mm in diameter and 76.2 mm long located at the center of the solenoid. The plastic frame for the solenoid (in our case, a polycarbonate tube with end-flanges made from acetal - also known as Delrin), and its placement relative to the vapor cell and other components, is depicted in Fig. S3. Copper wire (gauge 21 or 22 is appropriate) is wound around the frame in two layers, with 220 turns/layer. The current I needed is calculated using $\mu_0 N_t I = B_z \sqrt{L_s^2 + 4r^2}$, where N_t is the number of turns, μ_0 is the magnetic permeability of vacuum, and B_z is the magnitude of the desired axial magnetic field [10]. We need a current ≤ 1 mA to generate the desired B_z .

C. Suppression of stray magnetic fields

It is clear from the previous subsection that any small departure from collinearity between the laser propagation

direction and the applied longitudinal magnetic field results in a small component of the pump and probe beams causing a persistent undesired $\Delta m = 0$ cycling of some atoms between the $m_{F_g} = 1$ and $m_{F_e} = 1$ levels (Fig. 4(b) of the main article). This weakens our approximation to a three-level lambda scheme, with the extraneous levels causing a decrease in EIT contrast and a significant reduction of slow light effects.

Here, we describe how to suppress below 0.2 mG (less than 0.5% of the Zeeman field B_z) any stray magnetic fields in the entire laser-atom interaction volume - a cylinder of diameter equal to that of the probe beam and of length equal to that of the vapor cell. First, we degauss the mu-metal shields. Next, we use an optical method to accurately measure the low-level residual magnetic field in the laser-atom interaction region after the degaussing [11]. As a reference, typical high-end commercial gauss meters reliably measure magnetic fields down to 10-20 mG, but not below.

1. Degaussing the magnetic shields

The mu-metal sheets lose shielding effectiveness over a period of a few days, primarily owing to the mechanical stress created by removing and replacing the end-caps on the triple-shield when changing the optical setup inside the magnetic chamber. This is attributed to atomic dipoles becoming progressively magnetically locked together through their own interactions rather than through external fields. We therefore have to degauss the shields on days we take any data (and definitely each time we open the magnetic chamber, e.g., to use a different vapor cell).

To degauss the shields, we subject the mu-metal to a large AC magnetic field of which the magnitude is slowly lowered to zero. The large AC field will overcome the locked dipoles, forcing their alignment with the AC field. In our experiments, we use a cable wound around the layer of thermal foam (~ 80 turns over a length of ~ 20 cm) surrounding the innermost mu metal shield to supply the degaussing current (see Fig. S2).

The appropriate rate of decreasing the current is determined empirically. If not decreased optimally, residual fields continue to circulate in the innermost shield which can be detected, as discussed in the next sub-section. By repeatedly modifying and iterating the degaussing process to optimally suppress the residual field we determined an adequate degaussing procedure: We passed a peak current of 5 A through the cable which is slowly lowered over 1-2 minutes using a Variac; the current is reduced twice as slowly when under 200 mA.

2. Optical measurement of sub-mG residual magnetic fields

The residual magnetic field after degaussing may be measured using the well-known fact that the magnetic moment of an atom precesses around an applied magnetic field \vec{B} (this is known as Larmor precession) at the Larmor frequency ν_L , given by $h\nu_L = g_f\mu_B|\vec{B}|$ [1]. The constants g_f and μ_B are the Lande g-factor and Bohr

magneton, respectively.

If we illuminate the ^{87}Rb vapor with a single strong circularly-polarized beam, say σ^+ , propagating along the z -direction, tuned to the $F_g = 2 \rightarrow F_e = 1$ transition, and apply a small magnetic field B_z (i.e., the z -direction is the quantization axis), then, as described in detail in Sec. 3A of the main article, this beam optically pumps the atoms into the $F_g = 2, m_{F_g} = +1, +2$ magnetic sub-levels after illumination over a time-scale of milliseconds. Turning the strong laser beam off at this point allows the “spin polarization” of the sample to begin decaying via the mechanisms discussed in Sec. 3B of the main article. If the relaxing atoms are now illuminated by a very weak σ^+ probe beam, so weak that its effect on the ongoing atomic relaxation is negligible, then the probe absorption continually increases in time (and the transmitted power decreases) as the atoms relax toward ground sub-states with lower m -values. This is because the transition strength, and hence the absorption, for a particular $m_{F_g} \rightarrow m_{F_g+1}$ transition, increases as atoms move toward lower m_{F_g} -values (see Fig. 4(b) in the main article). The absorption settles to a steady-state value after a few tens of milliseconds, once the population distribution among the $F_g = 2$ magnetic sub-levels attains steady-state equilibrium.

Fig. S4(a) shows the result of a measurement of the probe absorption as a function of time, as described above. We use $B_z = 2.4$ mG, and illuminate the atoms with a single circularly polarized beam for which the intensity is modulated between two states, by sending a square-wave-modulation to the AOM (see Fig. 5 in main article): A high-intensity state (the pump phase), in which the beam is intense (4.3 mW/cm 2 in our case) for a period of 500 ms, followed by a low-intensity state (the probe phase) where the beam intensity is kept at 0.044 mW/cm 2 . The low-intensity state is at 500 ms

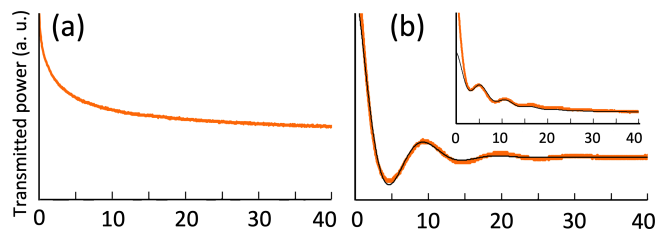


Fig. S4. a) Monitoring the sample depolarization with a weak σ^+ -probe, in the presence of a small solenoid current that applies an axial magnetic field of 2.4 mG. b) If the solenoid current is set to zero, the depolarization (and hence the absorption, see text) oscillates at the Larmor precession frequency ν_L which is determined by fitting the transmission with a decaying oscillatory function. We find that ν_L here corresponds to a stray field of 139 μG , which is a typical value obtained after degaussing. If the degaussing procedure is not optimized, the measurement yields a significantly higher ν_L -value (see inset) and therefore a higher residual magnetic field, 244 μG in the case shown here.

long, though only the first 40 ms need to be recorded (since, by that time, the population is distributed evenly among the ground state magnetic sub-levels and the absorption settles to a steady-state value, as can be seen in Fig. S4(a)). The switching-time between the two intensity-states is 15 μ s, which is much smaller than the time-scale over which the depolarization takes place.

However, if a stray non-axial magnetic field \vec{B} is present, the probe absorption shows oscillations, as shown in Fig. S4(b). If we set the solenoid current to zero during the measurement above so that the only contribution to a magnetic field in the z -direction comes from the z -component of \vec{B} , the atomic magnetic dipoles precess around \vec{B} at the Larmor frequency ν_L during the depolarization process, i.e., the projections on the z -axis of the magnetic dipoles precessing around \vec{B} oscillate at this frequency, as do the energy separations between the Zeeman sub-levels. The laser detunings for the transitions, and hence the populations, change in accordance causing observable oscillations in the sample absorption at ν_L . By measuring the oscillation frequency, we can determine the magnitude of the weak stray B -field from the expression for ν_L above. The plot in Fig. S4(b) corresponds to a stray magnetic field of 139 μ G.

The inset in Fig. S4(b) shows that this stray B -field measurement technique can be used to optimize the mu-metal shield degaussing procedure. In the example shown, persistent currents in the innermost shield lead to detectable Larmor oscillations in the absorption, corresponding to a residual non-axial magnetic field nearly twice as strong as the typical case depicted in the main plot in Fig. S4(b).

The measurements in Fig. S4 were performed in a vapor cell of isotopically pure ^{87}Rb with 30 Torr of Ne buffer gas (sample length $L = 51$ mm) warmed to 65°C (number density $\sim 3.8 \times 10^{11}/\text{cm}^3$). At the time this measurement was performed we happened to have this particular vapor cell in the magnetically shielded chamber. We do not expect the results in Fig. S4 to be significantly different if we had instead used the 10 Torr vapor cell on which all the data in the main article was collected.

D. Heated alkali vapor cell and cell-holder:

The most direct method to increase the density N of the atoms participating in EIT is to raise the temperature of the alkali vapor cell. Following the Novikova group at College of William and Mary [12] we directly wound an electrically insulated non-magnetic heating wire (see Fig. S2) around the outer surface of the innermost mu-metal shield, for heating the entire volume of space enclosed by the innermost shield. The heating wire was coated in a thermal paste to improve thermal contact with the shield. The wire is held firmly in place with thermal tape and a layer of thermally insulating foam.

The vapor cell is held in a pair of plastic holders (in our case, acetal). The vapor cell fits securely inside a lip on each holder, as shown in Fig. S3(b) and (c). A rubber

O-ring is placed in the lip on each end of the cell to prevent the cell from jostling around. The holders are a close slide-fit inside the solenoid frame. The vapor cell should be heated uniformly, so that “cold spots” due to thermal gradients do not occur on the cell. Holes are drilled through the body of the cell holders, as shown, to allow heated air to circulate, which significantly reduces the time needed for heating and increases the uniformity of the heating. To accurately control the cell temperature, the heating wire current is controlled by reference to a thermocouple placed near the cell. During data-taking, we turn the heater off to prevent any extraneous magnetic fields arising from the heater current.

An empirical equation for the pressure p of Rb vapor in thermodynamic equilibrium with its solid phase is [13]:

$$\log_{10} p = -94.04826 - \frac{1961.258}{T} - 0.03771687 \times T + 42.57526 \times \log_{10} T \quad (\text{S24})$$

where T is in Kelvin, and p is the vapor pressure in Torr. Assuming the ideal gas law holds, we write:

$$N = \frac{133.3 \times p}{k_B T}. \quad (\text{S25})$$

Here the factor 133.3 converts from Torr to Pa and k_B is the Boltzmann constant. Fig. S5 shows a plot of the number density versus vapor temperature, which is useful while designing EIT and slow light experiments.

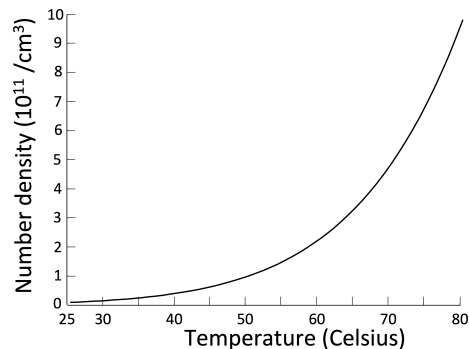


Fig. S5. Number density N versus vapor temperature T for Rb.

S3. Price and vendor list for key components

Table 1 provides a price and vendor list for all the key components of the experiment. Expensive items such as the external cavity tunable diode laser system (ECDL), and the mu-metal magnetic shield with degaussing capability, can be built in-house to cut costs [8, 14, 15]. In addition to some basic optics, the SAS setup [16] (see Sec. 4C of the main article) requires a simple uncoated vapor cell (natural abundance Rb, no buffer gas) which can be purchased from Precision Glassblowing (model TG-ABRB) for \$350.

Table 1. Key components used for the slow light experiment.

Item	Model	Cost
ECDL, current/temperature control	Vitawave (Russia) ECDL7940R	\$ 8000 [14, 15]
Anamorphic prism pair	Thorlabs PS871-B	\$ 164
Faraday Rotator	Conoptics 712B	\$ 1985 [17]
PM single mode fiber	Thorlabs P3-780PM-FC-2	\$ 197
Fiberport for each end of fiber (2)	Thorlabs PAF2A-11B	\$ 587 each
Cage assembly for telescope	Thorlabs CP33 (plate); SR4 (rods)	\$ 211
AOMs (2)	Gooch and Housego 3080-122	\$ 660 each
Dual channel waveform generator	Rigol DG4102	\$ 899
RF amplifier (Gain 30 dB)	RF-Bay MPA-22-30	\$ 330
Glan-Thompson polarizer	Newlight Photonics Inc. GSC 0108	\$ 549
Polarizing beamsplitters (3)	Thorlabs PBS 252	\$ 253 each
Nonpolarizing beamsplitter	Thorlabs BS 013	\$ 225
Half-wave plates (8)	Singapore Optics WP-05UM-LH-795	\$ 95 each
Quarter-wave plates (4)	Singapore Optics WP-05UM-LQ-795	\$ 95 each
Photodiode	New Focus Inc. 1621	\$ 594
Triple mu-metal shield & degauss wire	Magnetic Shield Corporation ZG-206	\$ 2130 [8]
Heater wire (15 ft)	ARi Industries 2HN063B-13	\$ 6.67/ft
Temperature controller	Omega CN743	\$ 115
Thermocouple	Digikey 317-1305-ND	\$ 3.18
Vapor cell for EIT and slow light	Precision Glassblowing TG-ABRB-I87 (pure ^{87}Rb , 10 Torr Ne)	\$ 650

[†] These two authors contributed equally.

* Corresponding author: balis@miamioh.edu

References

- P. W. Milonni and J. H. Eberly, “Laser Physics”, Wiley (2010), Sec. 9.10, pp 441 - 446
- This can be seen by considering the Lorentz force in Gaussian units: $\vec{F} = e(\vec{E} + \vec{v}/c \times \vec{B})$, where \vec{E} and \vec{B} have the same dimensions. The second term is negligible when $v \ll c$.
- For a spatially extended sample illuminated by a *plane* electromagnetic wave propagating in the z -direction, the field \vec{E} incident on an atom located at z has a spatial phase e^{ikz} . This spatial phase can be included in the Rabi frequency which is defined immediately after Eq. (S7). However, note that the result for the polarizability α_p in Eq. (S19) depends only on $|\Omega_c|^2$, i.e., α_p is the same for all the atoms in the sample. Hence, it is justified to use Eq. (S19) in the macroscopic expression Eq. (S20) in order to obtain Eq. (S22) and Eq. (S23).
- See Sec. 8.2, pp 332 - 334 in Ref. [1]
- H. J. Metcalf and P. van der Straten, “*Laser Cooling and Trapping*”, Springer-Verlag New York, Inc (1999)
- M. Lukin, M. Fleischhauer, A. Zibrov, H. Robinson, V. Velichansky, L. Hollberg, and M. Scully, “Spectroscopy in dense coherent media: Line narrowing and interference effects”, *Phys. Rev. Lett.* **79**, 2959 - 2962 (1997)
- OD in the main article is related to the factor ηkL in Ref. [6] (see Eq. (2) therein): $OD = \eta kL(\Gamma/2)/\gamma_{13}$. The factor ηkL is just $N(3\lambda^2/2\pi)L$ where $3\lambda^2/2\pi$ is the resonant absorption cross-section for a single stationary atom (see Eq. (2.28b) in Ref. [5]).
- S. Dickerson, J. Hogan, D. Johnson, T. Kovachy, A. Sugarbaker, S. Chiow, and M. Kasevich, “A high-performance magnetic shield with large length-to-diameter ratio”, *Rev. Sci. Instr.* **83**, 065108 (1-9) (2012)
- On the other hand, if the electric field vector of the incident light field is along the z -axis, the induced transitions among the Zeeman sub-levels obey the selection rule $\Delta m = 0$, even though the pump and probe beams are ostensibly prepared in Sec. 4B of the main article as σ^+ and σ^- beams.
- E. Callaghan, S. Maslen, “The magnetic field of a finite solenoid” NASA Technical Note D-465, E-900, 1-26 (1960) (<https://ntrs.nasa.gov/citations/19980227402>)
- M. Shuker, O. Firstenberg, Y. Sagi, A. Ben-kish, N. Davidson, and A. Ron, “Ramsey-like measurement of the decoherence rate between Zeeman sublevels”, *Phys. Rev. A* **78**, 063818 (2008)
- N. B. Phillips, “Slow and stored light under conditions of electromagnetically induced transparency and four-wave mixing in an atomic vapor”, PhD thesis, College of William and Mary (2011)
- A. N. Nesmeyanov, Vapor Pressure of the Chemical Elements (Elsevier, Amsterdam, 1963), English edition edited by Robert Gary
- A. S. Arnold, J. S. Wilson, and M. G. Boshier, “A simple extended-cavity diode laser”, *Rev. Sci. Instrum.* **69** (3), 1236 - 1239 (1998), and references therein
- E. Brekke, T. Bennett, H. Rook and E. L. Hazlett, “3D printing an external-cavity diode laser housing”, *Am. J. Phys.* **88**, 1170 (2020)
- A. Hachtel, J. Kleykamp, D. Kane, M. Marshall, B. Worth, J. Barkeloo, J. Kangara, J. Camenisch, M. Gillette, and S. Bali, “An undergraduate measurement of radiative broadening in atomic vapor”, *Am. J. Phys.* **80** (8), 740 - 743 (2012); *ibid.* **81**(6), 471 (2013)
- This isolator has an advertised tuning range of 644 - 780

nm, but functions well at 795 nm (we measured -38 dB of isolation at 92% transmission). Conoptics models for 700 - 900 nm are 712GG and 713A.